공학박사 학위논문

# Advanced Process Control Using Plasma Information (PI-APC) for Improving Edge Uniformity of Capacitively Coupled Plasma Etcher

## 용량결합형 플라즈마 식각 장비의 가장자리 균일도 개선을 위한 플라즈마 정보 인자 기반 고급 공정 제어

2023 년 2 월


서울대학교 대학원

에너지시스템공학부

송 재 민

# Advanced Process Control Using Plasma Information (PI-APC) for Improving Edge Uniformity of Capacitively Coupled Plasma Etcher

지도 교수 김 곤 호

이 논문을 공학박사 학위논문으로 제출함
2023 년 2 월


서울대학교 대학원
에너지시스템공학부
송 재 민


송재민의 공학박사 학위논문을 인준함
2023 년 2 월

| | | |
|---|---|---|
| 위 원 장 | 정 경 재 | (인) |
| 부위원장 | 김 곤 호 | (인) |
| 위 원 | 박 설 혜 | (인) |
| 위 원 | 김 윤 하 | (인) |
| 위 원 | 김 남 균 | (인) |

Abstract

# Advanced Process Control Using Plasma Information (PI−APC) for Improving Edge Uniformity of Capacitively Coupled Plasma Etcher

Jaemin Song

Department of Energy Systems Engineering

The Graduate School

Seoul National University


The advanced process control based on plasma information (PI−APC) is developed to improve edge uniformity of $SiO_2$ mask on Si mold etch process in very high frequency driven capacitively coupled etcher for $Ar/O_2/SF_6$ plasma. In the PI−APC constructed with a cascaded double−loop structure, the plasma information (PI) variable has a key role as a bridging parameter that links these two loops. Especially, the PI variable with the slope form along with wafer radial direction is proposed to represent distribution characteristics determining etch process uniformity. Including these characteristics, the system for PI−APC essentially consists of (i) sensor to monitor the PI based on phenomenology, (ii) equipment component to be manipulated for varying the PI, (iii) model to predict process results, and (iv) algorithms to compute control action.

As the sensors for monitoring the slope of the PIs in two different positions, the bare probe array with two tips and the VI sensor connected through the power line of the bottom electrode are adopted for ion density and DC sheath potential at each.

Additionally, optical emission spectroscopy (OES) is adopted to monitor the fluorine and oxygen radical density with actinometry method. All these monitored PI parameters are candidates of the controlled variable for $SiO_2$ and Si etching process, known from the domain knowledge for a given equipment and target process. In other words, the control objective in targeted equipment and process determines PI sensors.

As the manipulated component, the edge ring, also called a focus ring is presented to actively control the plasma distribution near wafer edge. For active and in-situ manipulating, the edge ring is modified to be applied by RF power with simplified structured anodized aluminum. Depending on the RF frequency, the effective length defined by the region where the plasma distribution is affected by the RF power applied to the edge ring is determined. From three different RF frequencies of 400 kHz, 2 MHz and 9.8 MHz as used in this study, the RF power of 400 kHz and 2 MHz frequencies, which are lower and similar toe the ion frequency, affect the edge potential distribution with the effective length about 10 mm and 30 mm, respectively. With validation of relative gain array (RGA) analysis, the RF power at 2 MHz frequency is selected with providing the radial range criterion of 120 mm and 145 mm positions to determine the slope formed PI of ion energy flux. Controllable gain for the variation range of the ion energy flux slope depending on the RF power degree can be estimated by the power balance with the equivalent circuit model, with about $-5.15\times10^{11}$ $Vcm^{-3}W^{-1}$. It is due to that the sheath thickness distribution determined by the DC sheath potential distribution makes change of 60 MHz main RF power coupling distribution. In other words, with higher 2 MHz edge ring power, more 60 MHz electrode power coupling in the region covered with the effective length. This makes RF powered edge ring adjust the slope of the PI even from a given negative slope to positive slope.

Virtual metrology using PI variable (PI-VM) is used as the process model for $SiO_2$ mask and Si mold etching with selection PI features governing the process. As a common parameter, the ion energy flux is dominant feature to determine both the etch rate of $SiO_2$ and Si. The radical density is additionally selected as the second important parameter, which are the fluorine and oxygen radicals for $SiO_2$ and Si, of each. It means that etch process for both materials mainly performed by energetic ions, but for $SiO_2$, there is enhancement with surface activation by fluorine radical, and for Si, there is inhibition of oxidation by oxygen radial. Models from the PI−VM analysis describe both $SiO_2$ and Si etching process with linearized relation with summation of the multiple between selected features and its weightings.

Model predictive control algorithm is adopted to control as the control model for PI−APC. From the open loop set−point test, the dynamic model for the slope form of the ion energy flux is developed on the variation of the RF edge ring power with 2 MHz frequency. The dynamic model for plasma control loop is described with first−order dynamic response composed with the gain of $-3.27\times10^{11}$ $Vcm^{-3}W^{-1}$ and time constant of 2.02 sec. This model means that it takes about 2.02 sec to reach the set value of the PI from manipulating edge ring power, which is due to systematic speed including time for the formation of the ion energy flux distribution by changed edge ring power degree. For the process control loop, required etch rate to compensate difference of mask heights at two different position is calculated from PI−VM model with the specific prediction window of $k$, which is multiple value to sampling time of the MPC for plasma control loop.

With PI−APC operation, edge uniformity is improved from 80 nm to 4 nm for the $SiO_2$ mask height difference and 77 nm to 43 nm for the Si edge depth difference in real process. Although the mask height is set as a control target with resulting in about 95% improvement of the edge uniformity, the etch depth is also controlled with about 44% improvement. It is because the principal process parameter is shared with ion energy flux which is used as the controlled variable. Different degree of improvement can be deduced from uncontrolled radical density and aspect−ratio−dependent effect (ARDE) for mold profile. According to operation result of the edge ring power by PI-APC, there is slightly increasing operation along the process time. This operating characteristic reveals that there was a process drift making the slope of the PI low, indicating lowering ion energy flux at edge boundary than inner region.

The advanced process control based on the plasma information was developed with double loop structure and the model predictive control algorithm. It is key role for processing plasma-enhanced process for semiconductor manufacturing to use plasma information inherent in plasma distribution and process uniformity characteristics. Unlike with the previous research for uniformity control, PI-APC composed with the single input and single output (SISO) scheme with the specific variable identifying plasma distribution with the slope form. For development of plasma process controller, it should be preceded to model the plasma and process to figure out the dynamic properties of the given system. However, for the improvement of control performance with disturbance rejection ability, it is suggested from this thesis to consist multiple input and multiple output (MIMO) scheme for more complex process control. For this future work, system gains will be composed with matrix formation for each relation.

**Keywords : Plasma Information (PI), Advanced Process Control (APC), Virtual Metrology (VM), Plasma Etching, Edge Uniformity**
**Student Number : 2014-21422**

# Table of Contents

# List of Tables

# List of Figures

depending on the process prediction window, k shows optimal control condition with k = 20.

# Chapter 1. Introduction

## 1.1. Advanced Process Control (APC) for Plasma Process in Semiconductor Manufacturing

Advanced process control (APC) has been applied as a process management technology to increase yield in semiconductor manufacturing processes [1−3]. APC has enabled active regulatory and automated process management from conventional passive and rigid process management technology for a repeated process units such as Run, Lot, and Wafer. For development of APC, not only controller for process but also various monitoring and metrology techniques are involved into a system [4]. Typically, the APC has been applied to Run−to−Run (R2R) control in which the process is controlled inter runs [5].

Plasma−assisted process has high complexity with numerous process knobs due to plasma and surface reaction dynamics having multi−dimensional and multi−scale characteristics [6]. This makes the APC have more than a single loop structure. Figure 1.1 shows the adjusted configuration of the APC for plasma−assisted process intertwined based on the existing configuration of the semiconductor process for Run−to−Run (R2R) application [4]. By adopting virtual metrology (VM) in semiconductor manufacturing, APC for R2R has been developed with partially substituting VM for real metrology [7−10]. For the plasma−assisted process, the plasma information (PI) parameter should be included.

To monitor the PI variables, proper sensors, and algorithms to calculate the PI from raw sensor data should be implemented to APC system, as represented with red dotted box in Figure 1.1. Through the PI variable, process is predicted, and plasma control algorithm is driven. Unlike existing VM based on equipment, FDC, and raw sensor data, by including PI variable in VM, so called PI−VM, the process can be predicted with improved accuracy with considering plasma phenomenon in given equipment [11].

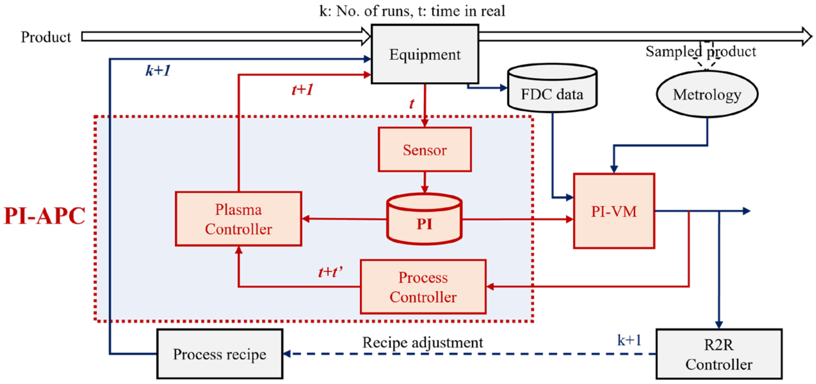


Figure 1.1. Real−time advanced process control scheme utilizing plasma information and virtual metrology.

## 1.2. Plasma Information (PI) based Dual-Loop Process Control Scheme

In the structure of the PI-APC, the controller computing and adjusting to required variance of the MV and PI variable by using predicted process variable, is shown in Figure 1.2. Since the ultimate control target of the PI-APC is to maintain the stability of the process result or to complete to given process target in time, the PI parameter is determined by the predicted process variable in real-time. In addition, there is relatively different dynamic characteristics of the equipment variable to PI parameter and process result value accumulated by surface reaction rate. Therefore, the structure of the plasma-assisted process controller is composed with intertwined structure of the plasma control and process control loop [12]. This structure is also called a cascade structure [13] depending on the different sampling time of each loop, and in general, process control loop determines final control target have a longer sampling time.

The plasma control loop performs control to reach and maintain a desired plasma state by changing manipulated variable of the actuator in equipment. Considering the error between the current state of the PI variable, $n_{n^*,measure}(0,t)$ in time, $t$ and the set value of that, $n_{n^*,target}(0,t+k\Delta t)$ in next time, the variance of the MV is determined and execute a control action. With interlocking with process control loop, the PI variable is set with updating new set value of the process variable. During the process time without updating process variable, the plasma controller still operates to maintain newest set value.

The process control loop performs control to regulate process results in real-time with determining set value of the PI variable. In the process control loop, the current status of the process variable is predicted with PI-VM model and compared with target value set in advance, such as etch depth and process time. Due to the target is given with length scale of the process, the process result is calculated by multiplying the rate and given sampling time.

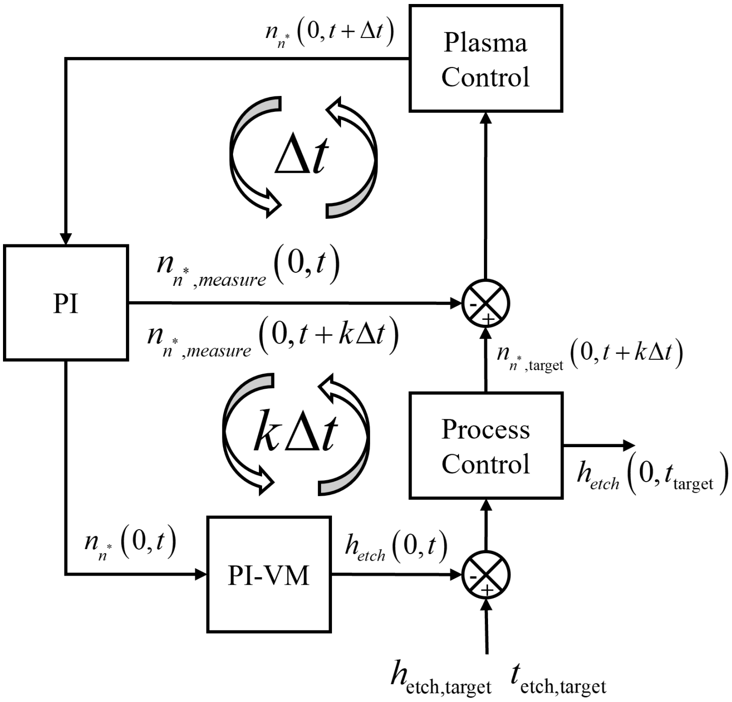


Figure 1.2. Dual-loop control scheme for plasma-assisted process.

### 1.3. High Aspect Ratio Etching Determined by Mask Shape

Mold structure as a target material of etch process has a certain pattern such as hole and trench which is transferred from mask pattern covering on mold surface [14−16]. Depending on the kind of product and design structure, the pattern and material of the mask is differed. Usually, for high aspect ratio (HAR) etch profile with narrow critical dimension (CD) and high etch depth, high energy ions and narrow angle distribution is required. This harsh process condition makes hard to maintain mask during HAR etching process. To withstand its shape for transferring ideal pattern, amorphous carbon material has been used as mask material. In other words, mask having collimating role to transfer energetic ions and neutral without distorting energy and angle distribution function defined in sheath region should be controlled for HAR etching process, as represented in Figure 1.3. Therefore, the mask shape (height and width) should be controlled as well as profile shape.

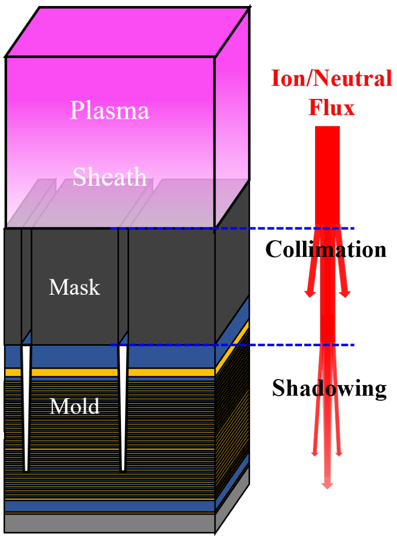


Figure 1.3. Mask transferring etch pattern with collimating ion/neutral flux into mold region and shadowing of incoming flux in high aspect ratio structure.

## 1.4. Previous Research for Etch Uniformity Management

To improve process uniformity, several research have been studied with various management knobs for etch equipment in semiconductor manufacturing industry. By dividing gas flow zone of gas distributor in equipment, the feeding gas flow rate is adjusted to control gas concentration distribution [17,18]. On the bottom electrode, wafer is placed, the temperature distribution can be controlled by susceptor heater adjustment [19,20]. These methods focused on chemical surface reaction. Variation of the gas concentration and surface temperature in mixed gas condition affects to all the reaction correlated with source gas species, which require complex control techniques. For controlling sheath potential structure, effect of the design of edge ring, also called as focus ring, has been researched in point of its geometry [21] and materials [22]. Although, these design parameters cannot be adjusted during processing, small change of height, angle and dielectric constant make change of sheath potential structure near wafer boundary, showing feasibility of local control knobs for edge uniformity management. In this study, by assigning active knobs to control sheath potential structure near wafer edge region, the edge ring is used as manipulating parts for real−time process control.

# Chapter 2. Experimental Details

## 2.1. Capacitively Coupled Plasma Etcher with RF Powered Edge Ring

The experiments to investigate the effect of the RF powered edge ring on plasma distribution and etch uniformity were carried out with capacitively coupled plasma (CCP) etcher equipment consisting of several parts, sensors, and diagnostic tools, as shown in Figure 2.1. The CCP etcher with a narrow gap generates the plasma by a very high frequency (VHF, 60 MHz) power. For improving process uniformity, a narrow gap distance between the showerhead electrode and the silicon wafer on the bottom electrode is set to 22.5 mm. Sigle frequency RF power was delivered to the bottom electrode through an RF matching system. Several low and middle frequency RF powers were delivered to the edge ring connected with vacuum RF feedthrough on the side. The operation pressure was constantly set with 20 mTorr both for single Ar and mixed gas with Ar, $SF_6$, and $O_2$ for etching process.

Non-invasive sensors and invasive diagnostic tools for obtaining plasma information (PIs) were installed, carrying out measurement with various positions of the equipment. Optical emission spectroscopy (OES, Avantes Avaspec ULS-2048L, 2 channel spectrometer) sensor was set to receive the emitting light of the plasma through a quartz optical window. Voltage-current (VI, Lab-made) sensor was set to receive the waveform of the RF voltage and current flowing power rod connected to bottom electrode. Langmuir probe (tungsten tip, 2.5 mm length and 0.2 mm diameter), with RF chock filter for eliminating RF oscillation, collected the ion and electron currents with probe bias. Retarded energy analyzer (RFEA, Impedans Vertex) obtained surface potential (floating potential) and the ion current filtered through 3 parallel grid structures on collector electrode depending on the ion energy.

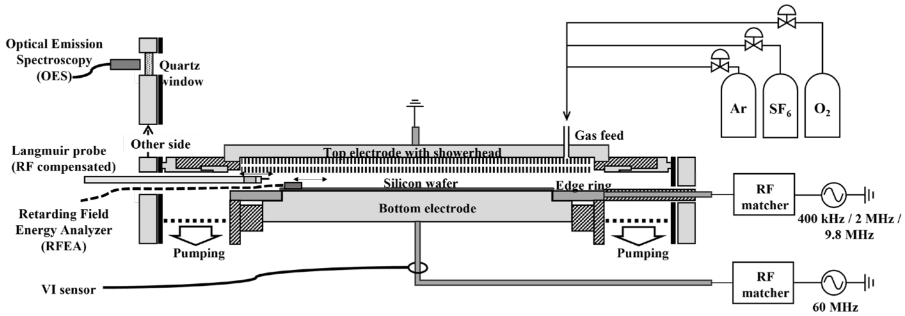


Figure 2.1. capacitively coupled plasma etch with Rf powered edge ring.

In the narrow gap CCP with VHF power, the radial plasma density distribution can be divided into four regions based on the generation and diffusion physics of the plasma, as shown in Figure 2.2. From wafer center to chamber wall, regions are distinguished depending on shape of density profile and dominant physics. In region 1, from wafer center to certain radial position about 50 mm, plasma density can be peaked with local electron heating by PSR-SWE resonance resulting in non-uniform distribution in center above specific VHF power [23-26]. In region 2, from the boundary of the region 1 to wafer radius, plasma density distribution is dominated by diffusion property with uniform source assumption following heuristic solution of the diffusion problem [27. 28]. In region 3, from wafer radius to outer radius of edge ring, plasma density distribute with diffusion from inner region and uniform ionization rate due to deviation from powered electrode. In this region, plasma density decreases with radial direction even having large slope. In region 4, from outer radius of edge ring to chamber wall, there are not direct applied power but accumulation of long-life particles such as metastable identifying grounded chamber wall as third electrode leading to virtual source of plasma [29].

In this study, the region of interest is near the boundary of the edge ring and wafer where the plasma density decreases in radial direction leading to low etch rate at wafer edge. Note that, there can be also etch profile tilt by sheath potential distribution caused by the slope shape of density distribution.

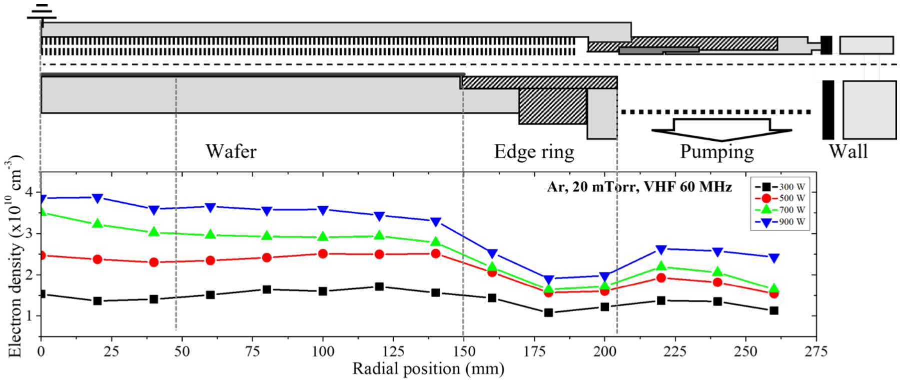


**Figure 2.2. Plasma distribution of VHF−CCP with four divided regions by governing transport physics.**

For electrical connection with auxiliar RF power source, edge ring which is also called focus ring was specially made of bulk aluminum, but with oxide coated layer on surface to prevent un−wanted electric connection with other parts, which is called anodizing treatment. However, it can be coupled with other parts with RF wave transmission due to the anodized coated layer can only insulate electrical DC component. Figure 2.2 shows cross−section view of the edge ring, used in this study, surrounding bottom electrode and wafer. Unlike usual structures used in other commercial equipment, it has plat top plane without any slope to exclude sheath potential curvature by geometrical effect.

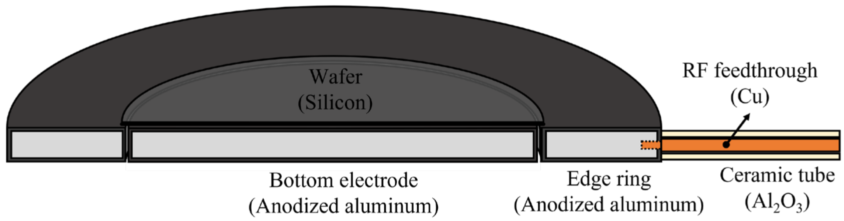


**Figure 2.3. RF powered edge ring made of aluminum with anodized coating layer.**

## 2.2. Sensors for Plasma Information with Distribution

For monitoring ion density distribution in real−time, an array of two cylindrical Langmuir probes is placed at the radial edge position of 120 and 145 mm from the wafer center where the ion density distribution has a slope near the boundary between wafer and edge ring. Two cylindrical probe tips were constructed from tungsten wire (diameter 0.2 mm, length 2.5 mm). To avoid the shadow effect by probe shaft, these tips were placed enough out of the floating sheath area, 5 mm away from the main ceramic shaft body, as shown in Figure 2.4 (a).

An electric circuit for biasing voltage and measuring current at two different tips was constructed as shown in Figure 2.4 (b). Each probe tips were biased with amplified dc voltage through amplifier circuit consisting of single operational amplifier (PA15A, APEX) and two resistors; the voltage gain was defined by the ratio of these resistors. Current signal at the probe tip was measured through isolation amplifier (AD210, Analog Devices) amplifying differential voltage drop across the reading resistor (500 Ω). Voltage signal was only measured at one of the two tips through amplifier circuit constructed with one isolation amplifier and two different resistors. Ion currents was monitored in real−time with probe bias of −50 V which was smaller than the floating potential about 4 V. The probe bias voltage was applied enough to avoid the effect of RF oscillation without RF chock filter. For the validation of the same measurement area of probe tips, I−V curve data acquired from each probe were confirmed by the similar shape and the difference between measured ion current was in about 3.2 % range at the same measurement position and condition. The operation procedure of the probe sensor is shown in Figure 2.5 (b). For eliminating the base current signal due to stray circuit component, offset of the current signal is calibrated at first. Then the probe voltage is applied to both probe tips. After measuring both ion current at a time, the ion density is calculated.

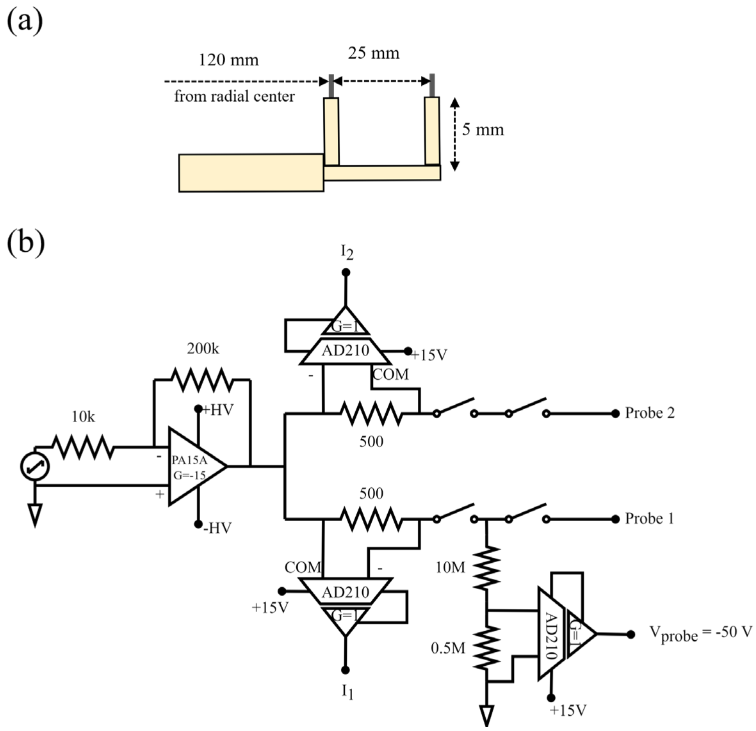


Figure 2.4. (a) Probe typed sensor with two positional tips and (b) electric circuit for real-time monitoring of each current at both probes.

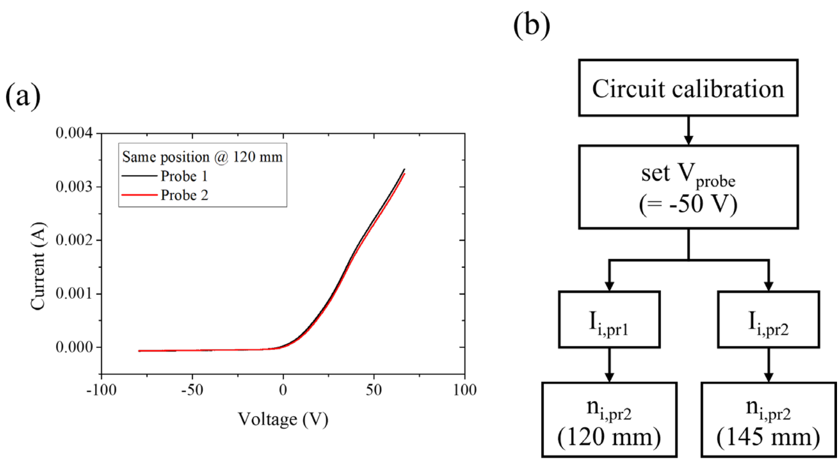


Figure 2.5. (a) Validation of probe areas with two different probe tips and (b) operating procedure of probe type sensor.

For monitoring discretized sheath potential distribution in real-time, VI sensor is installed covering RF power feed line of the bottom electrode. From the oscillating RF voltage signal, the dc component of the sheath potential is determined from Equation (2.1) and (2.2) based on the Kohler's capacitive voltage division model [30, 31]

$$\overline{V}_{sh} = -\frac{T_e}{2}\ln\left(\frac{2\pi m}{M}\right) + T_e \ln I_0\left(\left(1-\rho_c\right)\frac{e\widetilde{V}_{RF}}{kT_e}\right) \tag{2.1}$$

$$\rho_c = \frac{1}{1 + C_w / C_t} = \frac{1}{1 + \left(\frac{A_w}{A_t}\right)\left(\frac{\overline{s}_t}{\overline{s}_w}\right)} \tag{2.2}$$

where, $\overline{V}_{sh}$ is DC sheath potential, which is also called 'self-bias voltage', $\widetilde{V}_{RF}$ is oscillating RF voltage obtained from VI sensor, $T_e$ is electron temperature. Here, $\rho_c$ is expressed as a function of the electrode area, $A_w$ and $A_t$, and the average sheath thickness, $\overline{s}_t$ and $\overline{s}_w$.

From monitored RF voltage signals and pre-obtained plasma density and electron temperature, the dc sheath potential was expected. Assuming that the dc sheath potential on overall wafer region is mainly defined by 60 MHz RF voltage and on wafer near the edge ring is defined by 2 MHz RF voltage flowed from the edge ring, the measured RF voltage signal was distinguished with FFT analysis to 60 MHz and 2 MHz signal intensity. In other words, the dc sheath potential on the position of 120 mm was expected with the 60 MHz voltage signal and 145 mm with 2 MHz voltage signal. Figure 2.6 (a) and (b) shows that it is confirmed that there are linear correlation between the expected sheath potential and the measured one by RFEA. The operation procedure above description is represented with Figure 2.6 (c).

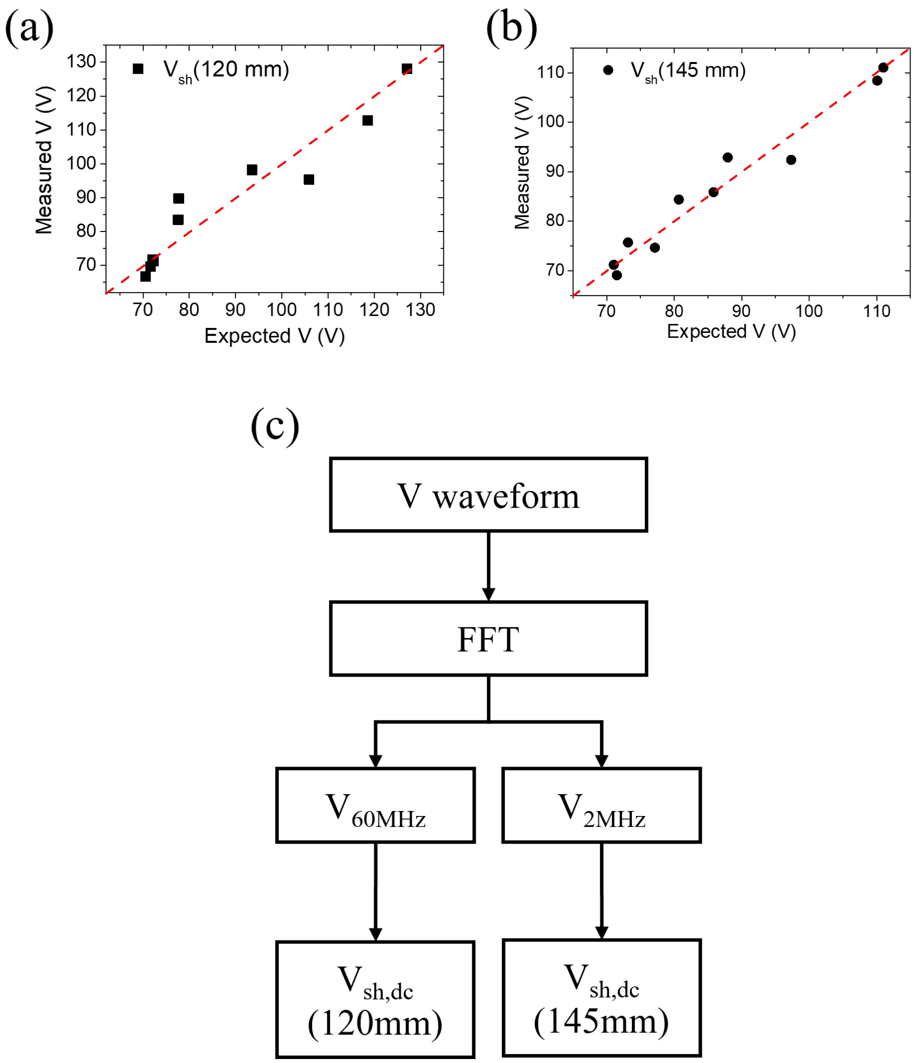


Figure 2.6. Correlation between surface potential measured by RFEA and 2 MHz filtered RF voltage from VI sensor at the radial position of (a) 120 mm and (b) 145 mm and (c) operating procedure of Vi sensor for potential distribution.

The actinometry method measured the fluorine and oxygen radical density in bulk plasma [32]. The concentration of neutral atoms emitting light with a specific wavelength by the transition of the excited state can be obtained from the intensity line ratio of two atomic lines which is shown in the following relation. The F neutral radical density, $n_F$ and $n_O$ is analyzed with

$$n_F = C_{Ar}^{F} n_{Ar} \frac{I_{\lambda=703.8\,nm}^{F}}{I_{\lambda=750.4\,nm}^{Ar}} \tag{2.3}$$

$$n_F = C_{Ar}^{O} n_{Ar} \frac{I_{\lambda=777\,nm}^{O}}{I_{\lambda=750.4\,nm}^{Ar}} \tag{2.4}$$

where, $C_{Ar}^{F}$ and $C_{Ar}^{O}$ are the actinometric coefficient, $n_{Ar}$ is the argon gas density and $I_{\lambda}^{X}$ is the intensity of the emission light from the X atoms with the wavelength, $\lambda$. The actinometric coefficient is defined by the ratio of the reaction rate and branching fraction of the transition. For a Maxwellian EEDF,

$$C_{Ar}^{X} = \frac{\Gamma_{Ar,i\to j}^{eff}}{\Gamma_{X,g\to k}^{eff}} \frac{k_{exc(g\to i)}^{Ar}}{k_{exc(g\to k)}^{X}} \tag{2.5}$$

where, $\Gamma_{X,a\to b}^{eff}$ is the effective branching ratio of the transition from a to b state, and $k_{exc}$ is the excitation reaction rate of the transition from ground, $g$ to $i$ state. The actinometric coefficient is a function of electron temperature assuming the Maxwellian EEDF because the variation of electron temperature with power is not serious for the whole etch processes. Then the values of 2 and 1.75 following from reference of [33] were adopted as the actinometric coefficient in monitoring the fluorine and oxygen radical density.

## 2.3. Etch Process Condition

The target process of this study is silicon (Si) mold with trench patterned silicon dioxide ($SiO_2$) mask. Figure 2.7 shows the detailed target pattern structure with dimension. $SiO_2$ mask has aspect ratio about 10 with 2,400 nm height and 235 nm critical dimension (CD) of trench pattern (Figure 2.7 (a)). Figure 2.7 (b) shows the top view of the trench. The trench length is about 5 mm with about 21 times larger than CD which is long enough to be assumed as infinite space in the direction of trench length. Pristine pattern is shown in Figure 2.7 (c) with space about 1,200 nm between each trench and initial etch depth about 100 nm of Si mold which might be resulted from over etch in mask etch process in before. In measurement of Si mold etch depth after etching process in this study, the initial etch depth should be considered.

Coupon having trench patterns is installed on the base Si wafer placed on the bottom electrode. From the full patterned wafer, the coupons were cut with 7 × 7 mm size square including trench and hole patterns, as shown in Figure 2.8 (a). To prevent the effect of sheath curvature at edge of the coupon structure resulting in unwanted distortion of the ion direction, bare Si wafer pieces were installed surrounding all sides of the square coupon (Figure 2.8 (b)). Between the bottom of the coupon and base Si wafer, silicon cement was pasted to guarantee heat and electric connection. In wafer region, the coupons were installed in three different positions, 0, 120, and 145 mm referenced by wafer center.

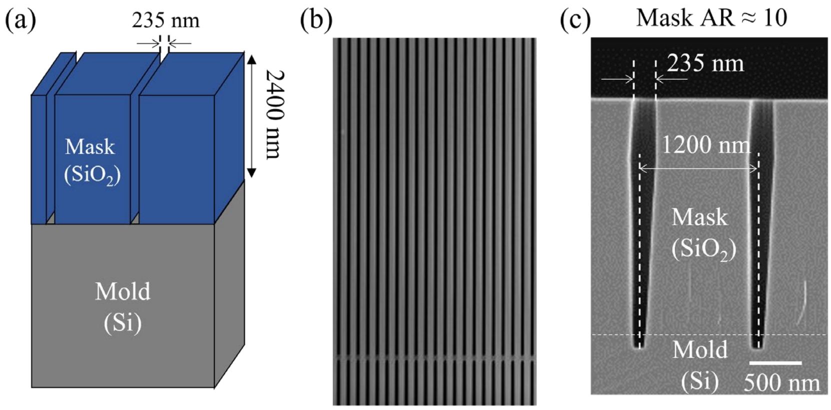


Figure 2.7. (a) Specification of process target with trench patterned silicon oxide mask and Si mold with its (b) top and (c) cross−section view by SEM image.

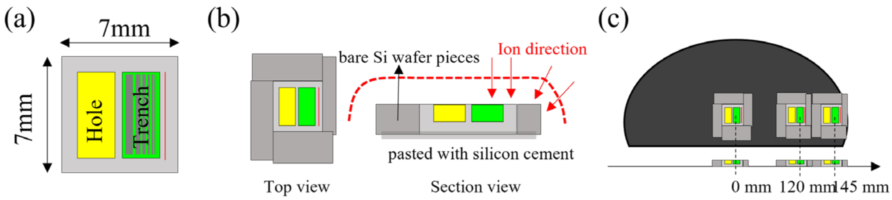


Figure 2.8. (a) Coupon type specimen with size about 7 mm × 7 mm and (b) installation method to prevent from sheath curvature by coupon thickness (c) with three different radial position, 0 120 and 145 mm on the wafer electrode.

Etching process is carried out in CCP etcher with $Ar/SF_6/O_2$ mixed gas plasma with 60 MHz RF source power on the bottom electrode and 2 MHz RF power on the edge ring. The detailed process condition is shown in Table 2.1. To exclude the PSR-SWE effect on the density distribution, 60 MHz RF power was constantly applied with 500 W lower that the specific power revealing PSR-SWE effect, which was determined in advance. As a etching gas, mixed gas with fluorine containing $SF_6$, $O_2$ and Ar is used with constant operation pressure with 20 mTorr. Detailed value of the operation conditions is shown in Table 2.1.

Table 2.1. Etch process condition.

| Equipment parameter | Value |
|---|---|
| Bottom 60 MHz RF Power | 500 W |
| Etch ring 2 MHz RF Power | 0 ~ 150 W |
| Pressure | 20 mTorr |
| Ar flow rate | 50 sccm |
| $SF_6$ flow rate | 120 sccm |
| $O_2$ flow rate | 75 sccm |
| Process time | ~ 300 sec |

## 2.4. PI−APC System

For implementation of advanced process controller to CCP etch equipment, manipulating parts of equipment and sensors for monitoring PIs were systematically integrated with various real−time data communication methods. RF power supplied with 60 and 2 MHz frequency are connected with LAN cable to the main control PC. Probe current is sensed through Lab−made DAQ with analogue signal and is transformed into digital signal in PCI−PXI board (National Instrument) installed in the main control PC. VI sensor obtain voltage and current signal waveform through BNC cable in analogue signal by using oscilloscope (Tektronix, DPO 7104) connected with LAN communication to the main control PC. OES (Avantes, Avaspec ULS−2048L, 2 channel spectrometer) measures the emission light from the plasma through quartz optical window at sidewall of the equipment and sensing data is transmitted to the PC with USB communication.

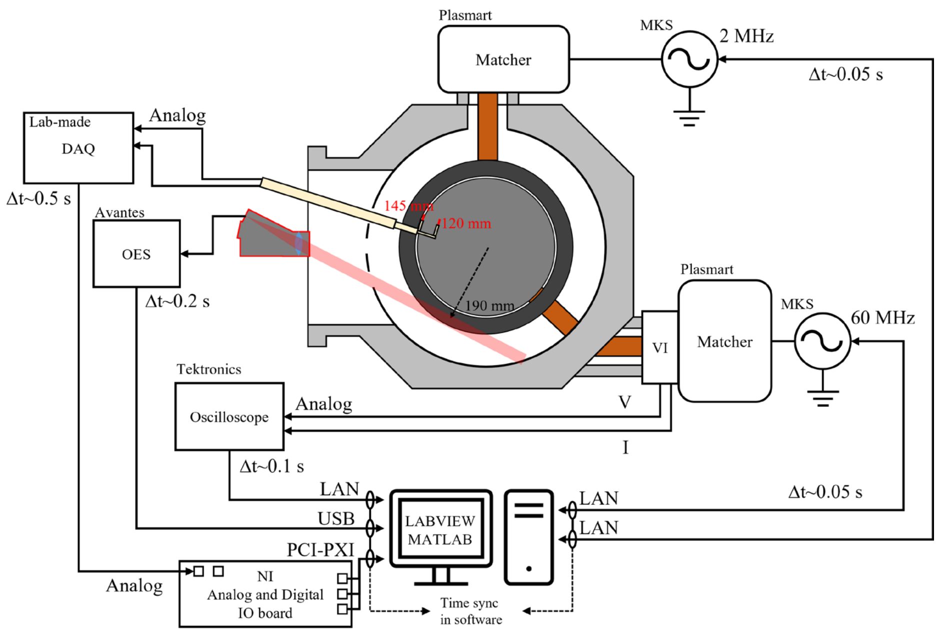


Figure 2.9. PI−APC system consisting of VHF−CCP etch equipment and PI uniformity sensors integrated in PC with LABVIEW® based software.

# Chapter 3. Characteristics of Plasma Distribution with RF Powered Edge Ring

## 3.1. Determination of Control Region with RF Frequency

Depending on the RF power specification on edge ring, plasma distribution in wafer region near the edge ring has different dynamic characteristics. Except for additional heating effect, low and medium frequency RF power were chosen as a power source on edge ring. These frequencies are in range of $0.05<\omega_{rf}/\omega_{pi}<10$, of which the low limit is enough to simulate low frequency RF sheath. For frequencies exceeding the above range, heating characteristics over the entire wafer region bay be affected. Even higher frequencies can exacerbate the plasma uniformity due to the formation of the standing wave. In this study, the effect of RF frequency on the plasma distribution is identified with three different frequencies, 400 kHz, 2 MHz, and 9.8 MHz.

Figure 3.1 shows the ion density distribution depending on the RF frequency of 400 kHz, 2 MHz, and 9.8 MHz and power degree on the edge ring in Ar plasma with 60 MHz main source power of 300 W. Compared with the ion density distribution without edge ring RF power, change of density distribution is clearly observed with higher frequency of 9.8 MHz. For 400 kHz and 2 MHz RF power, which are less or similar with ion plasma frequency of this condition, ion density distribution has been little changed within about 5% overall. However, for 9.8 MHz frequency about 3.8 times more than the ion plasma frequency, ion density has been increased with whole region, regardless of the power degree. This means that middle frequency of RF power on edge ring affect to plasma heating in overall region despite to the auxiliary power inducing to the electrode surrounding to the main electrode. It may be helpful to develop high density plasma source, but for improving plasma uniformity, middle frequency RF is not proper as an auxiliary power on the edge ring.

For DC sheath potential distribution, the RF frequency determined effective region. Figure 3.2 shows the measurement results of the DC sheath potential distribution for three different RF frequencies and various power. The edge region, where the edge ring bias affects the sheath potential, extends toward the radial center of chamber with respect to the increase of edge ring RF bias frequency. While the 9.8MHz bias applied to the edge ring affects the whole area on the wafer, 2 MHz bias only affects sheath potential near wafer edge(~125 mm). In the case of 400 kHz bias, the sheath potential on the wafer cannot be effectively changed by edge ring bias, and only the sheath potential on the edge ring, outside the wafer, is changed. This difference is caused by the difference of coupling mechanism between the edge ring and the bottom electrode. 9.8 MHz bias on the edge ring can be coupled directly with the bottom electrode to change overall sheath potential on the wafer. Meanwhile, 2 MHz and 400 kHz bias cannot be coupled directly to the bottom electrode and only penetrate to certain area from the wafer edge, which was defined as the edge area.

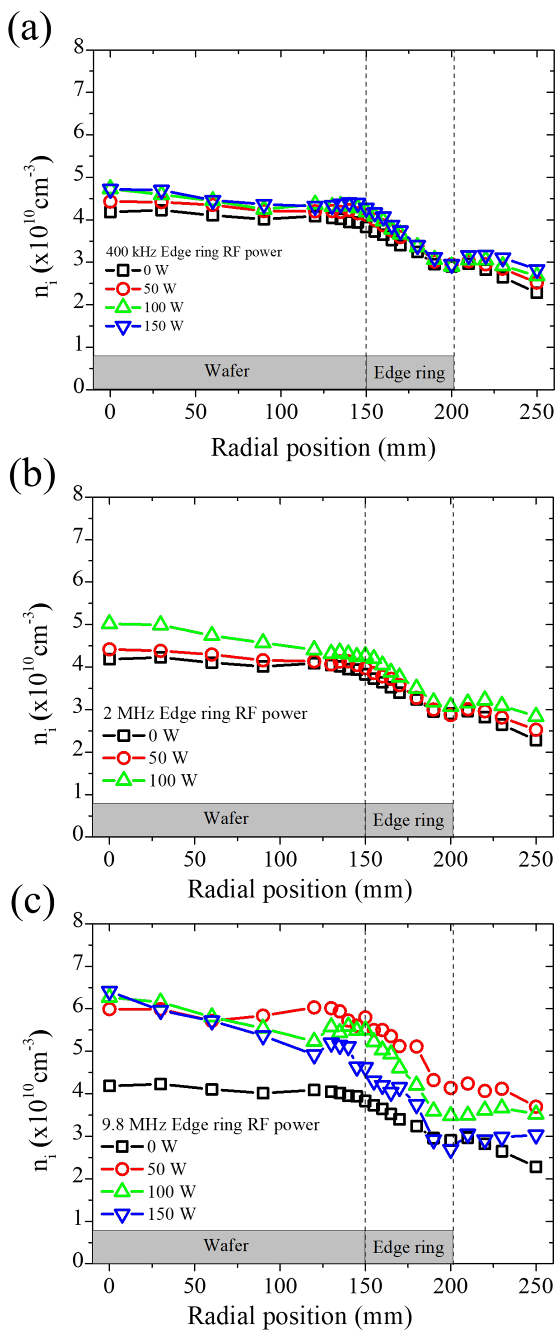


Figure 3.1. Ion density distribution measured by Langmuir probe in condition of RF frequency of edge ring about (a) 400 kHz, (b) 2 MHz, and (c) 9.8 MHz.

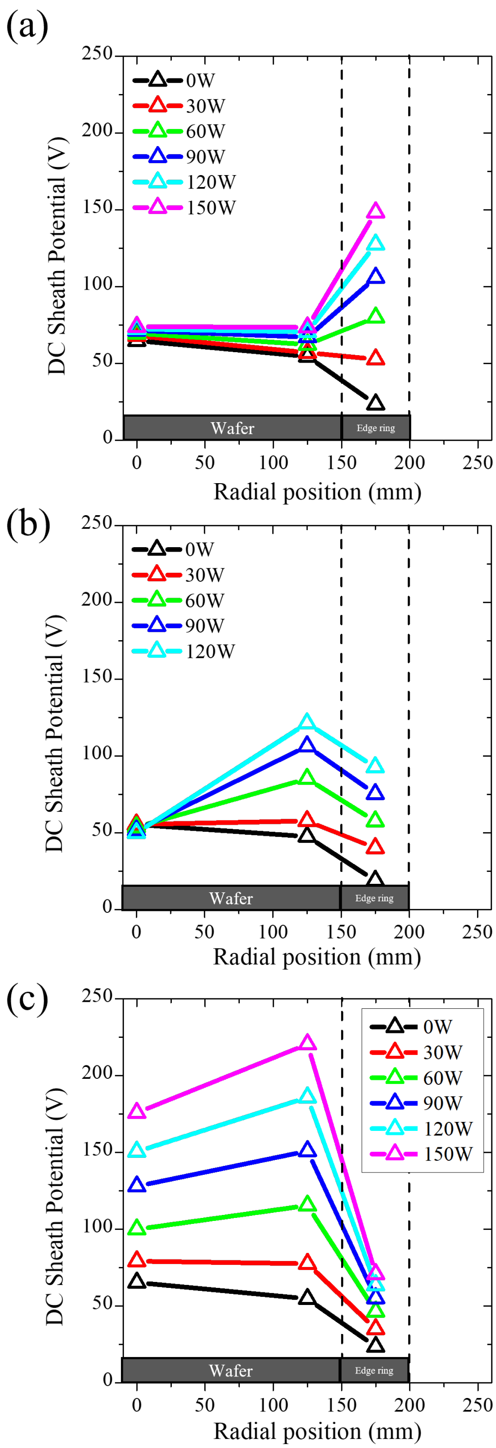


Figure 3.2. DC sheath potential distribution measured by RFEA at three radial positions with 0, 125, and 175 mm in condition of RF frequency of edge ring about (a) 400 kHz, (b) 2 MHz, and (c) 9.8 MHz.

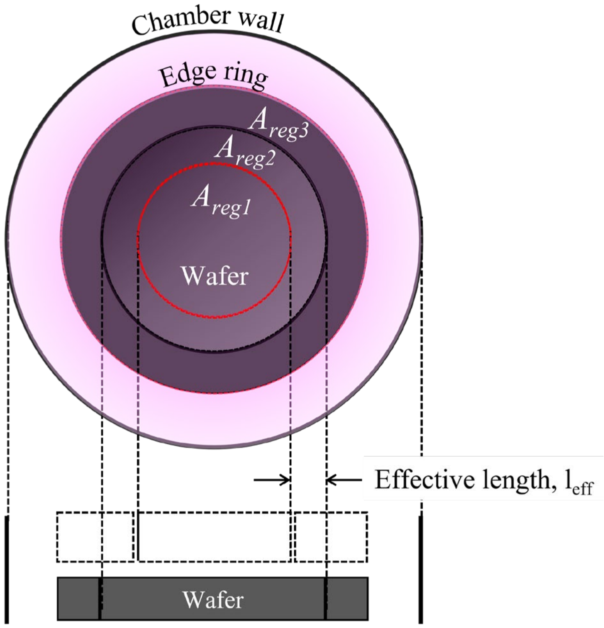

**Figure 3.3. Definition of effective length of RF power on edge ring about electron density and ion energy near boundary between wafer and edge ring.**

The effective length of the RF power on edge ring about electron density and ion energy can be determined from ion power balance with distinguishing two regions near the boundary between wafer and edge ring. Figure 3.3. shows the definition of the effective length, $l_{eff}$ in the schematic of the CCP with RF powered edge ring. To distinguish the effective area of the power balance for RF power on edge ring, plasma is divided by three different regions with considering boundaries of electrode and edge ring and virtual boundary defined by effective length. Region 1 is defined by the radial range of 0 to the virtual boundary, $R_{wafer} - l_{eff}$ . Region 2 is from the virtual boundary to the wafer edge, and region 3 is from the wafer edge to end of the edge ring.

Plasma absorbed power from edge ring can be distributed between the electron heating and the ion acceleration [34, 35]. Accounting for different electron heating mechanisms, the power ratio of electron power to ion power can be written as

$$P_{edge} = P_e + P_i = A_{eff,total} h_l u_B n_{e0} \left( \varepsilon_T + \bar{E}_{i0} \right) \tag{3.1}$$

$$r = \frac{P_e}{P_i} = \frac{S_{ohm} + S_{stoc} + S_{ohm,sh}}{S_i} \tag{3.2}$$

where, $S_{ohm}$ , $S_{stoc}$ and $S_{ohm,sh}$ are the energy fluxes due to the ohmic heating in the bulk plasma, the stochastic heating and the ohmic heating in the sheath respectively. $S_i$ is the energy flux due to ion acceleration in the sheath. These energy fluxes are represented as [24],

$$S_{ohm} = 2K_{ohm} \left( m / 2e \right) h_l \varepsilon_0 \omega^2 \nu_m T_e^{1/2} V_1^{1/2} d \tag{3.3}$$

$$S_{stoc} = 2K_{stoc} \left( m / e \right)^{1/2} \varepsilon_0 \omega^2 T_e^{1/2} V_1^{1/2} \tag{3.4}$$

$$S_{ohm,sh} = 2K_{ohm,sh} \left( m / 2e \right) \varepsilon_0 \omega^2 \nu_m s_m V_1 \tag{3.5}$$

$$S_i = 2K_V e n_e h_l u_B V_1 \tag{3.6}$$

where, $K_i$ are numerical constants corresponding to each power dissipation process [34], m is the electron mass, $\varepsilon_0$ is the vacuum permittivity, $h_l$ is $0.86\left(3 + d / 2\lambda_i\right)^{-1/2}$ , where $\lambda_i$ is the ion mean free path. $V_1$ is the fundamental rf voltage amplitude across a single sheath and $n_e$ is the electron density. $s_m$ is the maximum sheath width and $T_e$ is the electron temperature.

For argon discharges, equation (3.2) becomes

$$\frac{P_e}{P_i} = \left( \frac{\omega}{F \omega_{pi}} \right)^2 \left( 1 + \frac{K_{ohm}}{2K_{stoc}} \left( T_e / V_1 \right)^{1/2} \frac{h_l d}{\lambda_e} + \frac{K_{ohm,sh}}{2K_{stoc}} \frac{s_m}{\lambda_m} \right) \tag{3.7}$$

with parameter, $F$ as for argon,

$$F = \left( \frac{K_V}{K_{stoc}} h_l \sqrt{\frac{M}{m}} \right) \approx 20 \sqrt{h_l} \tag{3.8}$$

where, $\omega_{pi}$ is the ion plasma frequency and $\lambda_e$ is the electron mean free path. For this study, the power ratio between electron power to ion power of this study is shown in Figure 3.4. As shown in Figure 3.1 and 3.2, with low frequency RF power smaller than ion plasma frequency, most of the absorbed power is used to accelerate ions. For middle frequency about 9.8 MHz, the power ratio is about 1, which means the absorbed RF power is equally distributed to electron heating and ion acceleration.

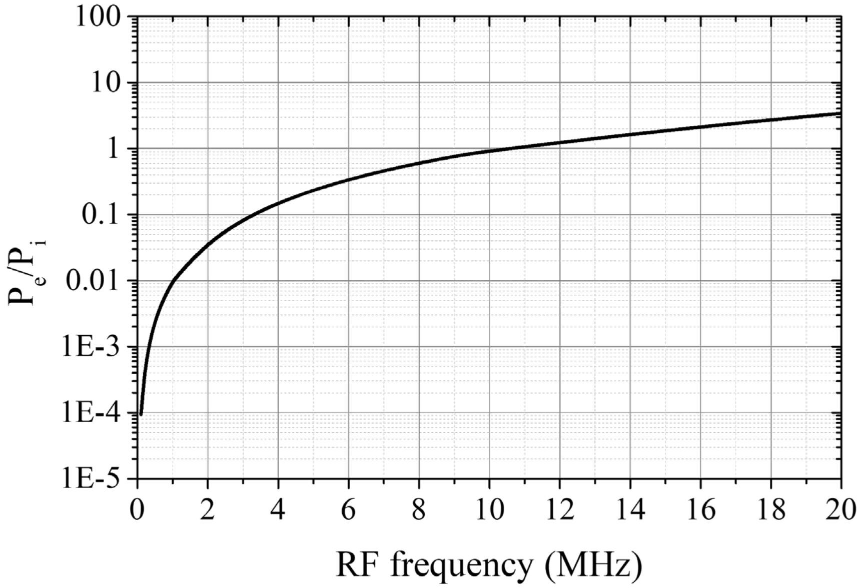


**Figure 3.4. The ratio of electron heating power to ion acceleration power depending on the RF frequency.**

To analyze the effective length by edge ring bias frequency, ion power balance model could be written as Equation (3.9) to link edge ring power and sheath potential near the edge ring.

$$\begin{aligned} P_{i,edge} &= A_{reg2} h_l u_B n_{reg2} \overline{E}_i + A_{reg3} h_l u_B n_{reg3} \overline{E}_i \\ &= h_l u_B \overline{E}_i \left[ n_{reg2} \pi \left( R_{wafer}^2 - \left( R_{wafer} - l_{eff} \right)^2 \right) + n_{reg3} \pi \left( R_{edge,out}^2 - R_{wafer}^2 \right) \right] \end{aligned} \tag{3.9}$$

where $P_{i,edge}$ is an absorption energy to ion, $A_{reg\,x}$ is an effective area in region $x$, $u_B$ is the Bohm speed, $n_{reg\,x}$ is an electron density in region $x$, and $\overline{E}_i$ is an ion acceleration energy. With considering the effective length, $l_{eff}$, the effective area of region 2 means rin shape with inner radius of shrink radius from wafer radius and outer radius of wafer size (150 mm). The effective area of region 3 is calculated with the same as the edge ring. The loss area for each region was set as top and bottom ring area.

From Equation (3.9), the boundary between region 1 and 2 can be obtained for different edge ring bias frequency as Figure 3.5. For 2 MHz bias, $l_{eff}$ is formed with 25 mm, and for 400 kHz bias, is formed with 5 mm, in accordance with radial sheath potential distribution data of Figure 3.2. From above analysis, by applying 2 MHz bias to the edge ring, the ion energy flux slope inside edge region can be effectively controlled by edge ring bias power.

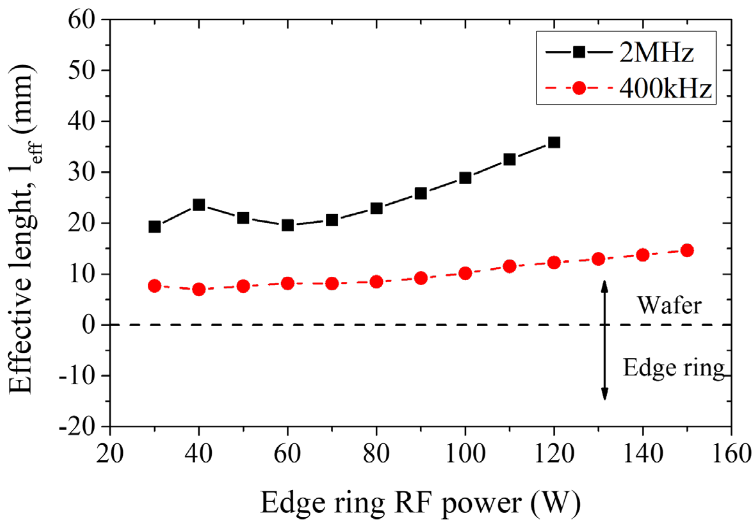


**Figure 3.5. Variation of the effective length with depending on RF power and frequency on the edge ring.**

The optimal actuator specification of the edge ring RF power for uniform ion energy flux can be determined with the contour map consisting with RF power ratio and frequency, as shown in Figure 3.6. Only with low frequency below the ion frequency about 2.5 MHz, the energy flux ratio representing plasma uniformity can be adjusted within variation of about 15 % applied power to main RF power.

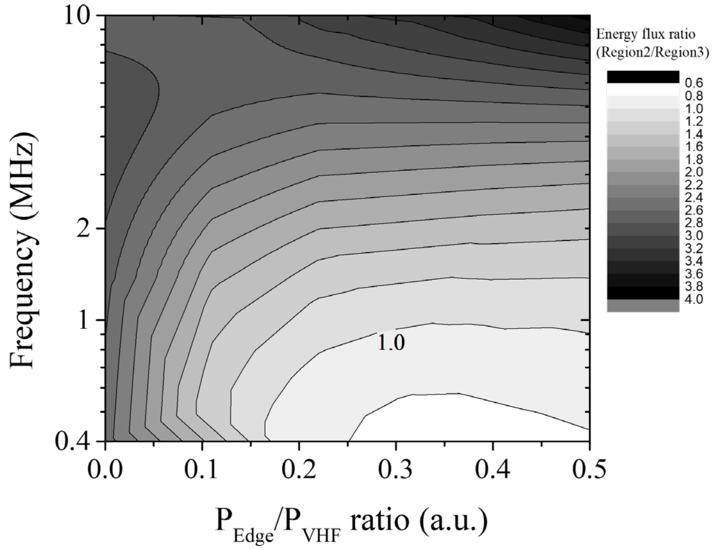


**Figure 3.6. Optimal condition for the uniformity between region 2 and 3.**

## 3.2. Validation of Controllability of RF Powered Edge Ring with RGA Analysis

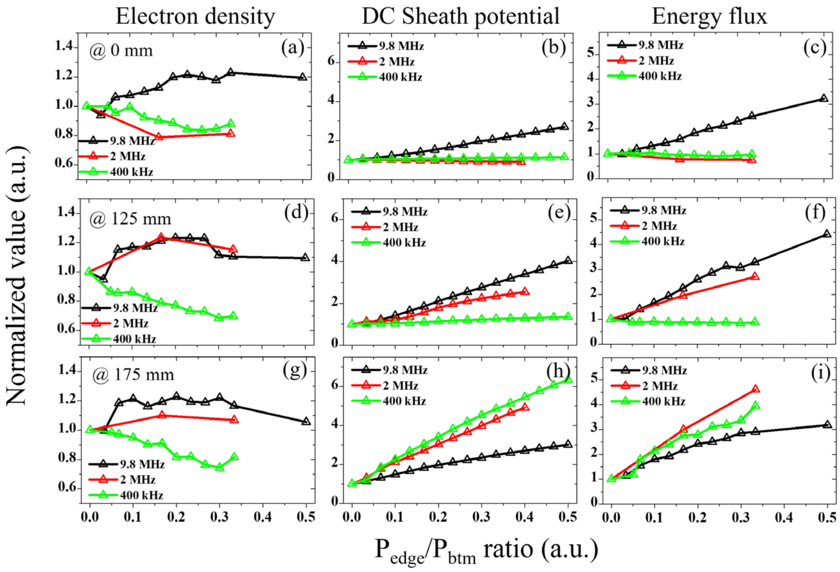


**Figure 3.7. Variation of electron density (a), (d), (g), DC sheath potential (b), (e), (h), and energy flux (c), (f), (i) with edge ring power variation for 400 kHz, 2 MHz, and 9.8 MHz RF frequencies.**

In the previous section, the plasma power balance model based on the physical analysis of the experimental data defined the radial region in the wafer which can be regulated by the RF power applied to the edge ring. It was confirmed that most of the RF power with lower than ion frequency is used for ion acceleration. And the lower the frequency, the shorter the effective length of the edge ring power. Based on these characteristics, the relative gain array (RGA) analysis method using experimental data with multivariable factors can be applied as a quantitative analysis method for selecting manipulated (MV) and control variable (CV) pairs.

RGA analysis method identifies the most effective pair of manipulated and control variable among the combinations of multiple inputs and outputs in multivariable control system, which enable to develop single-input single-output (SISO) control model [13, 36, 37]. As shown in Figure 3.7, the experimental data on the variation of the outputs of the electron density, DC sheath potential, and energy flux for three different measurement positions of 0, 125 and 175 mm with varying inputs of the RF power ratio on the edge ring to the bottom electrode with three different frequencies of 400 kHz, 2 MHz, and 9.8 MHz were used.

The steady-state gain matrix for the applied RF power on the edge ring with three different frequencies in each column and three different measurement positions is divided with row. The gain matrix for the DC sheath potential variable is shown in Equation (3.10), the electron density variable in (3.11) and the energy flux variable in (3.12).

$$\mathbf{K}_{V_{DC,sh}} = \begin{bmatrix} 1.05 & -0.09 & 0.07 \\ 1.57 & 1.05 & 0.19 \\ 0.40 & 0.97 & 1.08 \end{bmatrix} \tag{3.10}$$

$$\mathbf{K}_{n_e} = \begin{bmatrix} 0.90 & -2.36 & -0.56 \\ 0.83 & 1.65 & -0.57 \\ 0.45 & 2.88 & -0.53 \end{bmatrix} \tag{3.11}$$

$$\mathbf{K}_{\Gamma_E} = \begin{bmatrix} 1.90 & -1.50 & -0.11 \\ 2.18 & 7.34 & 5.50 \\ 0.60 & 5.50 & 0.83 \end{bmatrix} \tag{3.12}$$

For multivariable control system, the value of the relative gain ratio for two pairs of the steady-state gain is defined as Equation (3.13), and the matrix of relative gain for all MV-CV pairs is expressed as Equation (3.14).

$$\lambda_{ij} = \frac{\left(\partial y_i / \partial u_j\right)_u}{\left(\partial y_i / \partial u_j\right)_y} = \frac{\text{open-loop gain}}{\text{closed-loop gain}} \tag{3.13}$$

$$\Lambda = \begin{array}{c c} & \begin{array}{ccc} u_1 & \cdots & u_n \end{array} \\ \begin{array}{c} y_1 \\ \cdots \\ y_n \end{array} & \begin{bmatrix} \lambda_{11} & \cdots & \lambda_{1n} \\ \vdots & \ddots & \vdots \\ \lambda_{n1} & \cdots & \lambda_{nn} \end{bmatrix} \end{array} \tag{3.14}$$

The RGA has several algebraic properties and control properties. The sum of its each row or column is one so that it is normalized. Also, it is not affected by scaling and units of input and output variables because of its dimensionless characteristics. In addition, we can get information of control properties of the system; When $\lambda_{ij}$ is equal to 1, $u_j$ affects $y_i$ without any interactions. In $0<\lambda_{ij}<1$ case, the interaction effect has the same direction with the main effect. That is, the interaction assists $u_j$ in controlling $y_i$. In contrast, in $\lambda_{ij}<0$ case, the system becomes unstable. Thus, the first rule is to avoid negative elements, and the second rule is to select elements close to 1[13].

The relative gain array of the ion energy flux at three different region is calculated with below.

$$\Lambda_{\Gamma_E} = \begin{array}{c} \\ \Gamma_E(R_1) \\ \Gamma_E(R_2) \\ \Gamma_E(R_3) \end{array} \begin{array}{c} \begin{array}{ccc} P_{9.8MHz} & P_{2MHz} & P_{400kHz} \end{array} \\ \begin{bmatrix} 0.86 & 0.20 & -0.06 \\ 0.10 & 0.85 & 0.05 \\ 0.04 & -0.04 & 1.01 \end{bmatrix} \end{array} \tag{3.15}$$

According to the selection method, MV−CV pairs for 9.8 MHz power for region 1, 2 MHz power for region 2 and 400 kHz power for region 3 are selected as a proper pair.

## 3.3. Theoretical Plasma Model with RF Powered Edge Ring

Based on the characteristics of plasma distribution with RF power on the edge ring, plasma model can be developed to be used as model in control loop. From this theoretical model, control gain defined by the ratio of the variation of controlled variable (CV) over of manipulated variable (MV) can be estimated. In previous chapters, we can use RF power degree as the manipulated variable with constant frequency to control the difference of the plasma variable between two regions near edge boundary in wafer region, about 120 and 145 mm. If RF frequency is determined, it is assumed that the effective length is constant with RF power variation. In other words, the effective length can only be determined by RF frequency.

Figure 3.8. shows equivalent circuit model for capacitively coupled plasma with RF powered edge ring. There are three different electrode components, bottom, and edge ring electrode with coupling through gap capacitance between them and top electrode covering whole range from center to near chamber wall. The bottom electrode is sourced by 60 MHz main RF power, $P_{fwd,btm}$ through blocking capacitor, $C_{block}$. The edge ring electrode is sourced by 2 MHz power, $P_{fwd,edg}$ through the same blocking capacitor and coupled to chamber wall with impedance component, $Z_{wall}$. As a region of interest is two radial positions at 120 and 145 mm, between the top and bottom electrode, two parallel impedance components, each composed of two series sheath impedance on top and bottom sheath, $Z_{sh,tx}$ and $Z_{sh,bx}$ with $x$ is radial position. It is assumed that, by changing RF power on edge ring, only sheath impedance at r=145 mm and on edge ring region varied. The sheath impedance is assumed only capacitance component as below,

$$Z_{sh,k} = \frac{1}{\omega C_{sh,k}} = \frac{s_k}{\omega \varepsilon_0 A_k} \tag{3.16}$$

where, $\omega$ is the rf frequency of coupled power, in this model, 60 MHz, and $C_{sh,k}$ is the sheath capacitance of $k$ circuit component defined by the vacuum permittivity, $\varepsilon_0$, the sheath thickness, $s_k$, and the effective area, $A_k$. The sheath thickness determined by dc sheath potential, $\bar{V}_{sh,k}$ is assumed with Child−Langmuir law [24],

$$s_k = \frac{\sqrt{2}}{3}\lambda_{Ds}\left(\frac{2\bar{V}_{sh,k}}{T_e}\right)^{3/4} \tag{3.17}$$

where, $\lambda_{Ds}$ is the Deby length, $T_e$ is the electron temperature, and $\bar{V}_{sh,k}$ is the dc sheath potential induced at $k$ circuit component.

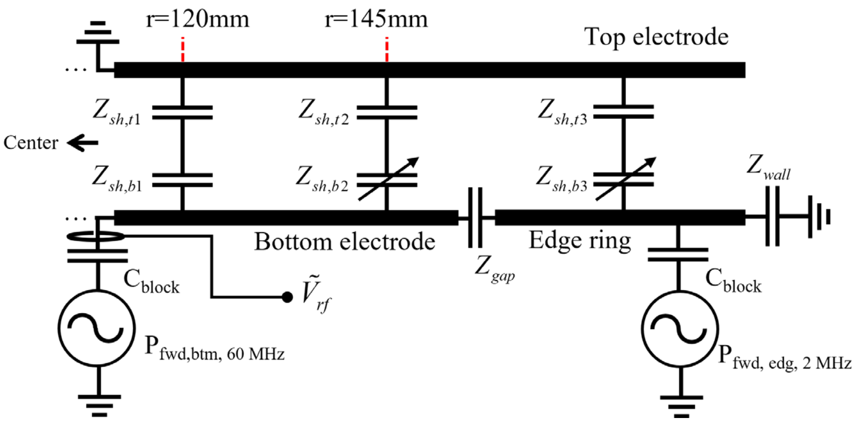


**Figure 3.8. Equivalent circuit model of capacitively coupled plasma with RF powered edge ring.**

The model based on the dc sheath voltage measured by RFEA with variation of 2 MHz RF power on edge ring. It assumed that induced RF power on the edge ring make change of surface potential distribution from edge to in wafer region defined by effective length in previous chapter. It is also confirmed by measured dc sheath potential at radical positions of 120 and 145 mm, as shown in Figure 3.9. From these results, it is expected that there can be two different operation regimes depending on induced RF power. Up to about 90 W of RF edge ring power, $V_{dc,sh}$ increased only at 145 mm with almost constant at 120 mm. However, when

RF power exceed 90 W, $V_{dc,sh}$ at 120 mm increased with more rapidly than at 145 mm. It is due to LF power induced on the edge ring coupled with the bottom electrode through the gap capacitance at more than specific power degree, in this case, about 90 W, which is about 18% of bottom electrode power.

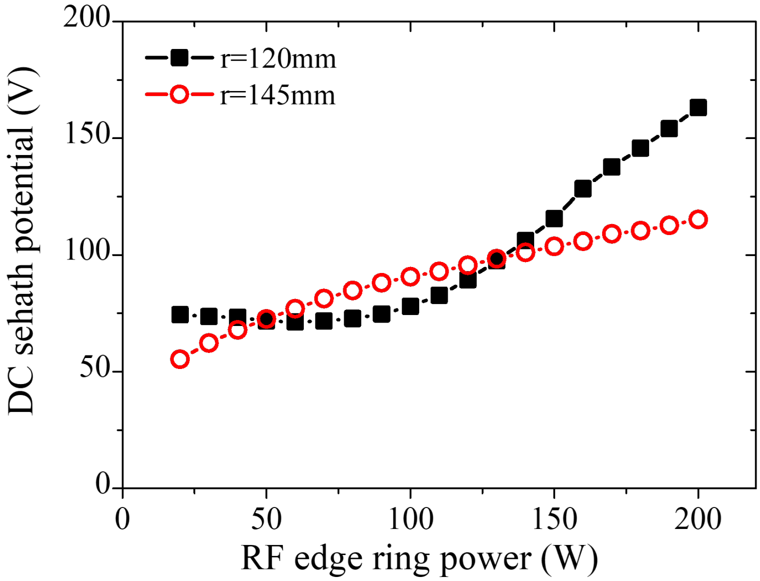


**Figure 3.9. Variation of dc sheath potential at 120 and 145 mm position measured by RFEA and Langmuir probe with RF power variation.**

Figure 3.10 shows schematic of power balance of this system with distinguishing two different region in wafer based on the effective length. Total main power absorption on both region is determined by the ratio of sheath capacitance, $Z_{abs}$ over total impedance including blocking capacitor,

$$P_{abs} = \alpha P_{fwd} \tag{3.18}$$

$$\alpha = \frac{Z_{abs}}{Z_{abs} + Z_{block}} \tag{3.19}$$

where, $\alpha$ is the power absorption efficiency. With assumption of only stochastic heating dominant plasma generation, absorption power is scaled with square of RF voltage of 60 MHz source power,

$$P_{stoc,k} \propto \frac{\omega^2 T_e^{1/2} A_k}{\varepsilon_c} \tilde{V}_{rf,60MHz} \tag{3.20}$$

where, $\tilde{V}_{rf,60MHz}$ is RF voltage induced on electrode and $\varepsilon_c$ is collisional energy loss. From this scaling, we can use divided RF voltage from total RF voltage which can be measured by VI sensor as divided power on each two distinguished regions, $P_{abs,1}$ and $P_{abs,2}$,

$$\tilde{V}_{sh,b1} = \frac{Z_{sh,b1}}{Z_{sh,b1} + Z_{sh,t1}} \tilde{V}_{rf,60MHz} \tag{3.21}$$

$$\tilde{V}_{sh,b2} = \frac{Z_{sh,b1}}{Z_{sh,b2} + Z_{sh,t2}} \tilde{V}_{rf,60MHz} \tag{3.22}$$

where, $\tilde{V}_{sh,b1}$ and $\tilde{V}_{sh,b2}$ are capacitively divided RF voltage induced from 60 MHz RF power on bottom electrode with region 1 and 2. Power balance model is assumed with that only 60 MHz RF power coupling is considered because low frequency and its low power degree could not directly affect to plasma generation(Figure 3.4. and 3.9.) and physical constant considered Ar plasma. Power balance equation is,

$$P_{abs,k} = en_{0,k} h_l u_B \sum_j A_{eff,j} \varepsilon_{T,j} \tag{3.23}$$

where, $P_{abs,k}$ is the absorption power at region $k$, $e$ is the elementary charge, $n_{0,k}$ is ion density at bulk plasma region, $h_l$ is the edge-to-center ratio, $0.86\left(3 + d/2\lambda_i\right)^{-1/2}$, where $d$ is the gap distance and $\lambda_i$ is the ion mean free path, $u_B$ is the bohm velocity, $u_B = \left(eT_e/M\right)^{1/2}$, where $M$ is the ion mass, $A_{eff,j}$ and $\varepsilon_{T,j}$ is the loss area and loss energy at region $j$. The energy loss per ion-electron pair created, $\varepsilon_T$ is defined by,

$$\varepsilon_T = \varepsilon_C + \varepsilon_e + \varepsilon_i = \varepsilon_C\left(T_e\right) + 2.5T_e + \bar{V}_{sh} \tag{3.24}$$

where, the collisional loss, $\varepsilon_C$ is $\varepsilon_{iz} + K_{ex}/K_{iz}\varepsilon_{ex} + \left(K_{el}/K_{iz}\right)\left(3m/M\right)T_e$, the electron power loss, $\varepsilon_e$ is $2T_e$ and the ion acceleration loss energy, $\varepsilon_i$ is $0.5T_e + \bar{V}_{sh}$.

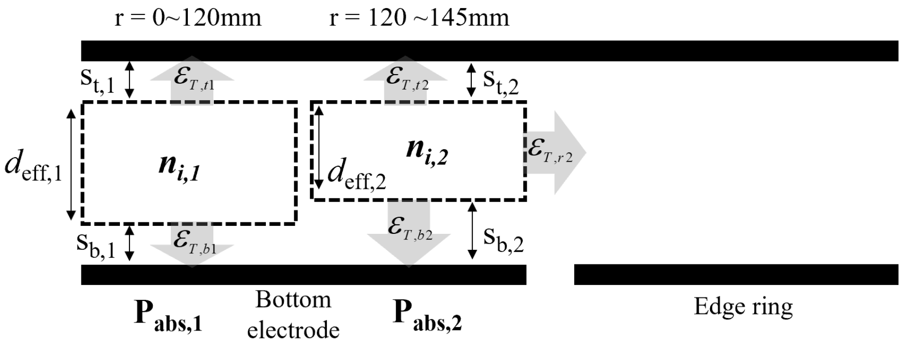


**Figure 3.10. Power balance of two discrete plasma region in wafer edge region with different sheath thickness.**

With these equivalent circuit model and power balance, ion density at two different regions can be calculated with measured dc sheath potential varied with RF power on edge ring. In other words, RF power on edge ring make change dc sheath potential distribution on edge ring as well as in-wafer region into the effective length. This potential distribution change induces sheath thickness distribution near the edge boundary, occurring re-arrangement of main power coupling depending on the radial position. It is confirmed with RF voltage and current signal measured from VI sensor at the bottom electrode. Figure 3.11 shows that FFT filtered RF voltage and current with 60 and 2 MHz frequency from VI sensor waveform with varying only 2 MHz RF power on the edge ring.

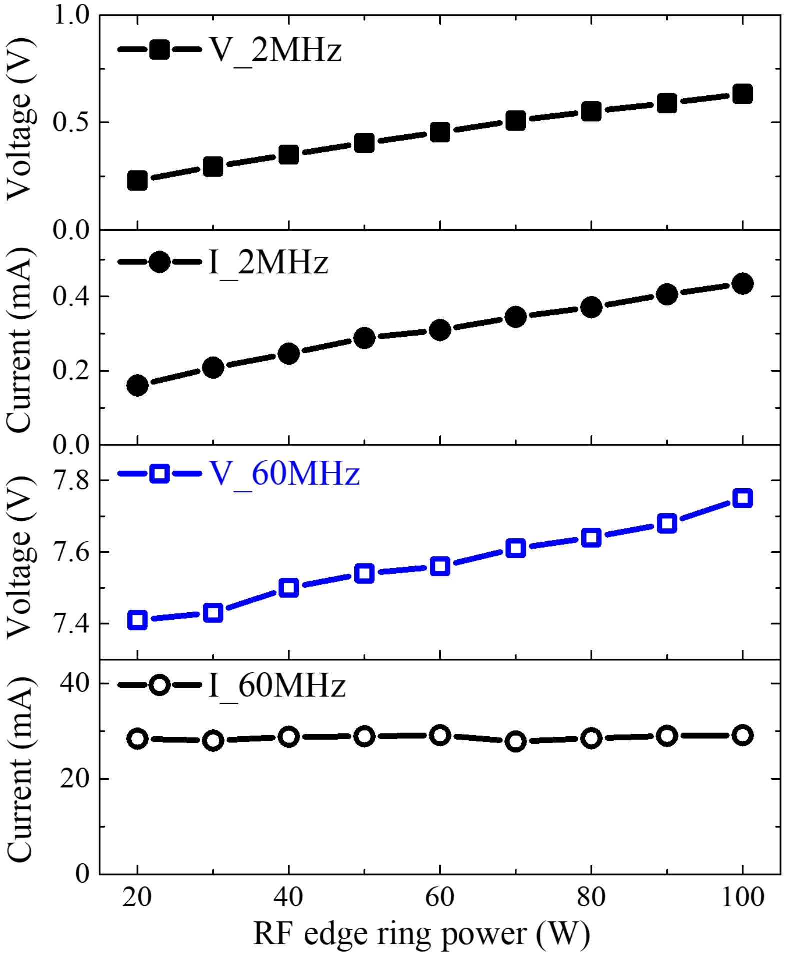


Figure 3.11. RF voltage and current signal extracted with FFT filter with 2 and 60 MHz frequency measured by VI sensor installed at the bottom electrode.

Figures 3.12 and 3.13 show that the calculated results of ion density and ion energy flux variation depending on the RF power on edge ring. With edge ring power variation inducing electrode power coupling model, ion density at both regions increases with increasing edge ring power degree, while the difference between two regions also increases. However, with considering ion energy defined by dc sheath potential, the variation of the ion energy flux variable has an intersection point between the variables of two different regions, which make direction of the radial difference variable. Therefore, within variation range below about 20 % of the edge ring power over the main electrode power (500 W), the difference at the edge region can be controlled with bi−directional operation.

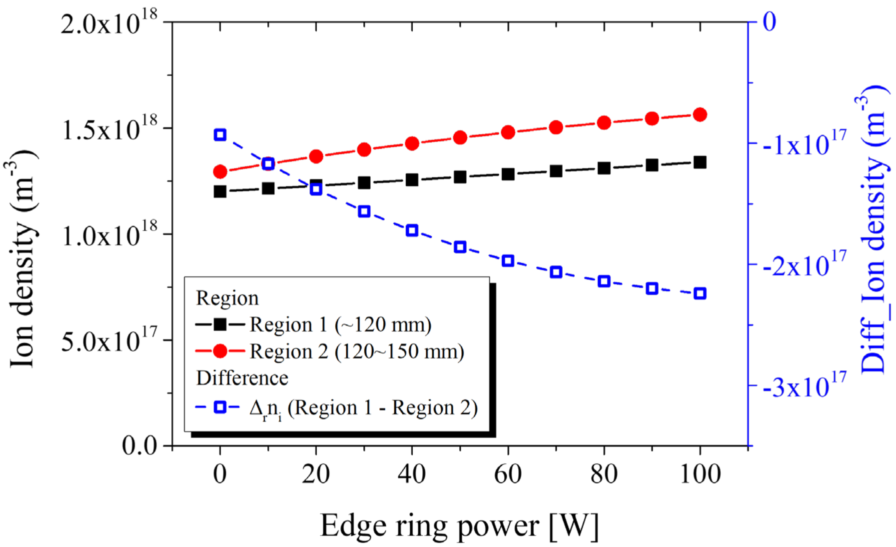

Figure 3.12. Calculated ion density at each region and difference of ion density between two regions.

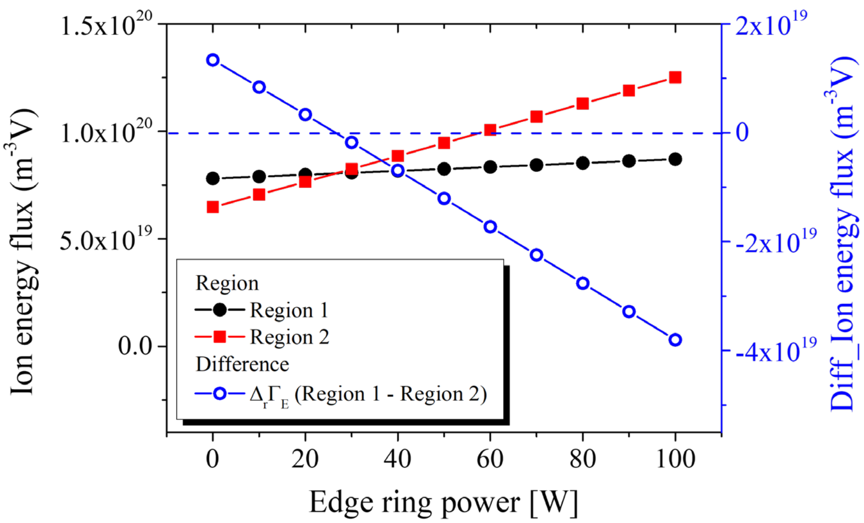

Figure 3.13. Calculated ion energy flux at each region and difference of ion energy flux between two regions.

# Chapter 4. Characteristics of Etching Process for Trench Patterned $SiO_2$ Mask and Si Mold

## 4.1. Virtual Metrology using Plasma Information (PI-VM)

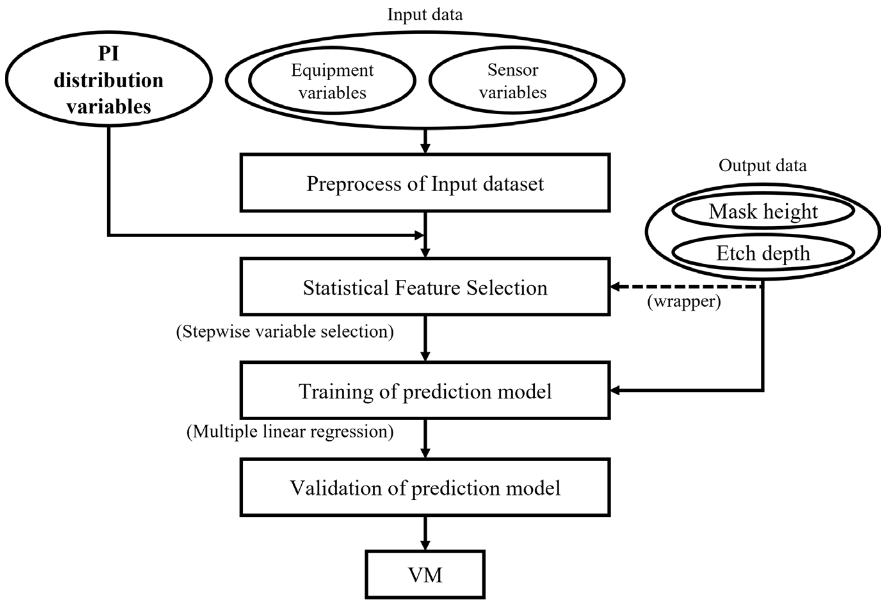


**Figure 4.1. Procedure of developing virtual metrology using plasma information variables.**

Figure 4.1 represents the procedure of PI-VM development [38, 39]. The first step of VM development is the preprocess of input dataset. Among the input data from equipment and sensors, meaningless data such as null value from equipment dataset is filtered and OES dataset has preprocessed with domain knowledge. After calibration of OES, the integration of the selected emission peak used to the following process step shown in figure, determination of PI variables and feature selection for the VM development.

With input data and PI variables (mentioned in previous session), the feature selection is carried out in next step. The stepwise variable selection (SVS) method is chosen, that was proposed by Jang et al. [38]. This method constructs suitable subset of the features from the input variables for multilinear regression, so called wrapper. The strengthen of this method is the combination of two separate stages, forward selection, and backward elimination. By repeating selection and elimination on the subset with increasing steps, the best combination of the features that contribute to improve the prediction is determined in terms of F−statistics [40].

Next is the training and validation steps. All of 48 datasets shown in Table 1 is used as the training dataset, determining the feature variables in this process. Statistical regression model, multiple linear regression (MLR), is adopted to build the linear relation between the selected features and output variables which is the process results. The regression model of MLR is given by

$$y_i = \beta_0 + \beta_1 x_{i1} + \cdots + \beta_p x_{ip} \tag{4.1}$$

where, $y_i$ is the $i$−th data of the output variable, $x_{ip}$ is the $i$−th data of the $p$−th feature, and $\beta_p$ is the regression coefficient for the $p$−th feature. The regression coefficients, $\beta_p$ are determined by training result. Based on these coefficients, the standardized regression coefficient is given by

$$\beta_p^{'} = \beta_p \frac{s_x}{s_y} \tag{4.2}$$

where, $s_x$ and $s_y$ is the standard deviation of input and output dataset. As indication of the relative importance of the features, the absolute value of the standardized coefficient can be used.

## 4.2. Process Model with PI−VM for Mask and Mold

Following the procedure for developing PI−VM introduced in previous section, the PI−VM model for the remain height of the $SiO_2$ mask and the etch depth of the Si mold target is developed. A total of 48 dataset were used for each process target to develop the PI−VM model. Each experimental input dataset consists of 24 kinds of EES data from RF matchers at the bottom electrode and the edge ring and 17 kinds of PI data measured from Langmuir probe and RFEA tools as shown in Table 4.1. Depending on the process condition with RF power degree applied on the edge ring and the position of the installed coupon, total 48 dataset were obtained from RF power variation with 12 condition and installation position varied with 4 different radial positions. Radial position was divided into 0, 120, 145 mm in wafer region and 175 mm on edge ring surface. Note that the etching at the 175 mm position is not interesting region in the actual process, but it is an effective position where the variation in sheath potential by manipulating RF power on edge ring is clearly shown, resulting in distinct variation of the etching characteristics due to varied ion energy.

Table 4.1. Input dataset used to develop PI−VM for remain $SiO_2$ mask height and Si mold etch depth.

| Category | Data source | Parameter |
|---|---|---|
| EES | RF Matcher at bottom electrode | $P_{Fwd,master}$ |
| | | $P_{Ref,master}$ |
| | | $C_{1,master}$ |
| | | $C_{2,mater}$ |
| | | $C_{3,master}$ |
| | | $S_{11,Re,master}$ |
| | | $S_{11,Im,master}$ |
| | | $V_{mag,master}$ |
| | | $I_{mag,master}$ |
| | | $Phase_{master}$ |
| | | $Z_{r,master}$ |
| | | $Z_{i,master}$ |
| | RF Matcher at edge ring | $P_{Fwd,edge}$ |
| | | $P_{Ref,edge}$ |
| | | $C_{1,edge}$ |
| | | $C_{2,edge}$ |
| | | $C_{3,edge}$ |
| | | $S_{11,Re,edge}$ |
| | | $S_{11,Im,edge}$ |
| | | $V_{mag,edge}$ |
| | | $I_{mag,edge}$ |
| | | $Phase_{edge}$ |
| | | $Z_{r,edge}$ |
| | | $Z_{i,edge}$ |
| PI | Langmuir probe | $V_p$ |
| | | $I_e$ |
| | | $T_e$ |
| | | $n_e$ |
| | | $I_i$ |
| | RFEA | $V_{dc\_surf}$ |
| | | $V_{dc\_sheath}$ |
| | Langmuir probe, RFEA | $V_{dc\_sheath}\Gamma_i$ |
| | OES | $n_e$ |
| | | $T_e$ |
| | | b factor |
| | | $n_F$ |
| | | $n_O$ |
| | | $n_{Ar,1s2}$ |
| | | $n_{Ar,1s3}$ |
| | | $n_{Ar,1s4}$ |
| | | $n_{Ar,1s5}$ |

The PI−VM prediction results for the remain $SiO_2$ mask height after etching process and the standardized coefficients of the selected features are shown in Figure 4.2. The PI−VM model with prediction accuracy of $R^2$=0.984 was developed (Figure 4.2. (a)) and two PI variables, ion energy flux [41, 42] and fluorine radical density variables, were selected as the feature representing etching model of $SiO_2$ mask (Figure 4.2. (b)). Considering that normalized coefficients of selected both features have negative values and that the prediction target of the process is the remain height value, both ion energy flux and fluorine radical play a role in etching the mask [43]. In other words, under the process condition in this study, $SiO_2$ mask is etched with energetic ions assisted with F radical reaction. Figure 4.3 also supports this etching mechanism with considering higher radical density in radial direction from the wafer center. It means that larger remain mask height (lower mask etch rate) at wafer center than at edge is caused by different F radical distribution. With similar radical density, the mask etch rate is increased with increasing ion energy flux variable.

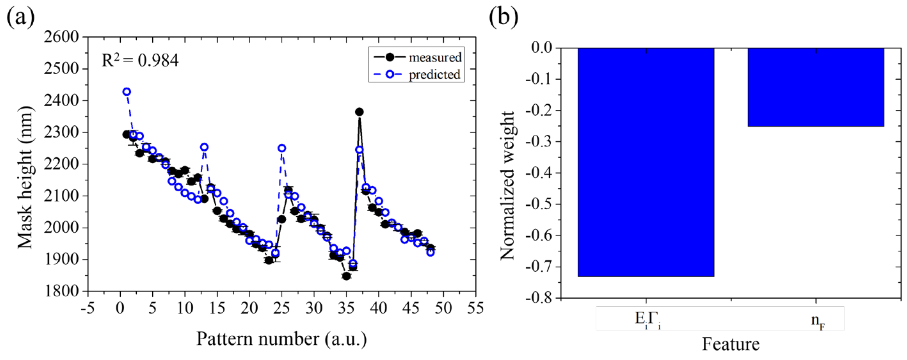


Figure 4.2. PI−VM result for SiO2 mask height with (a) predicted and measured values and (b) normalized weightings for the selected PI features consisting of ion energy flux and fluorine density variables.

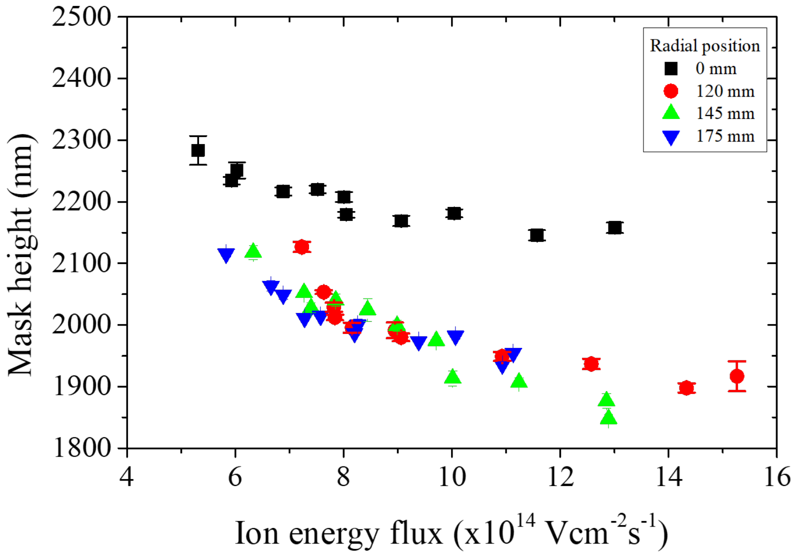


Figure 4.3. Linear correlation between ion energy flux and mask height of the process results depending on the radial position.

The PI−VM prediction results for the Si mold etch depth after etching process and the standardized coefficients of the selected features are shown in Figure 4.4. The PI−VM model with prediction accuracy of $R^2$=0.969 was developed (Figure 4.4. (a)) and two PI variables, ion energy flux and oxygen radical density variables, were selected as the feature representing etching model of Si mold (Figure 4.4. (b)). Considering that normalized coefficients of selected both features have positive value, the ion energy flux play a key role in etching Si mold and oxygen radical having negative valued coefficient plays a role in passivating. In other words, under the process condition in this study, Si mold is etched with energetic ions and inhibited with O radical reaction for formation of oxide or $SiOF_x$ layer.

The linearized models for the remain mask height and etch depth are described below with selected PIs and its coefficients. From the PI−VM models for etch depth of $SiO_2$ mask and Si mold with constant process times about 300 sec, process model for the etch rate of each target was developed with equation (4.3) and (4.4) divided process time.

$$\left(Mask\,height\right)\; h_{mask} = a_0 + a_1 E_i \Gamma_i + a_2 n_F \tag{4.3}$$

$$\left(Mold\,etch\,depth\right)\; h_{mold} = b_0 + b_1 E_i \Gamma_i + b_2 n_O \tag{4.4}$$

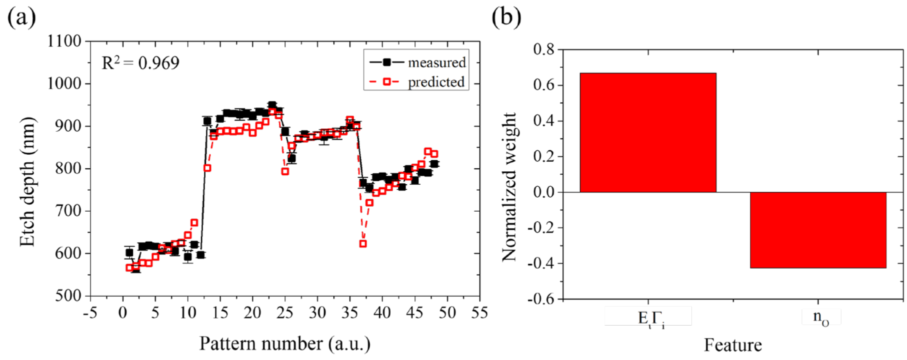


Figure 4.4. PI−VM result for Si mold etch depth with (a) predicted and measured values and (b) normalized weightings of the selected PI features consisting of ion energy flux and oxygen density variables.

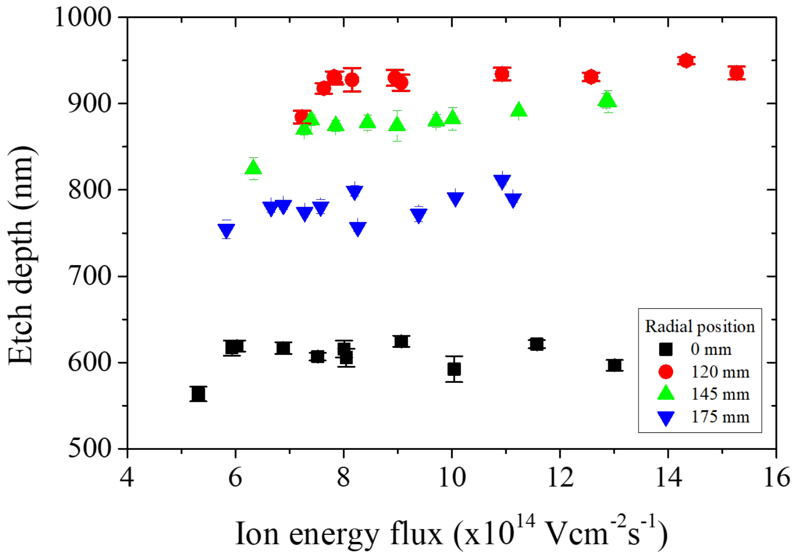


Figure 4.5. Linear correlation between ion flux and etch depth of the process results depending on the radial position.

# Chapter 5. Development of PI−APC for Improving Etch Uniformity

## 5.1. PI−APC Structure for Edge Uniformity Control

Plasma information based advanced process controller (PI−APC) for process uniformity consists of tangled two control loops for equipment−plasma and plasma−process at each. To construct the PI−APC structure, along with the control target, it is needed to develop additional sensor considering phenomenology of equipment−physics, select manipulated variable and controller variable pair, construct control and process model algorithm with domain knowledge or empirically and implement all of these to control system with hardware and software.

Major procedure for development of PI−APC is shown in Figure 5.1, based on the usual procedure [13]. In this study, the etch process edge uniformity in the capacitively coupled plasma etcher was taken as the control target. From the previous research, the edge ring parts surrounding electrode−wafer is selected as manipulated parts due to its dynamic operation capability with inducing RF power for changing potential distribution, as described in Chapter 1.4. For monitoring variables related to process uniformity, the plasma information especially with the formation of the difference in radial direction was considered. Special sensor for this PI was devised with Langmuir probe having two tips with different radial position, as described in Chapter 2. The plasma dynamic model was validated with theoretical model in Chapter 3. In Chapter 4, CV is selected as PI variable of ion energy flux for prediction of mask and mold etching process.

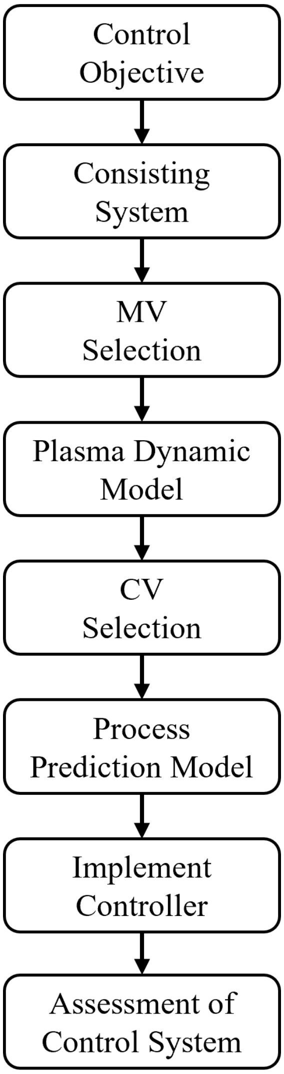

Figure 5.1. Major procedure of developing control system.

Figure 5.2 shows the constructed PI−APC structure with capacitively coupled etch including RF powered edge ring. Before operating controller, models for PI−VM and plasma control algorithm were uploaded to the system. From the beginning of the monitoring PI with ion energy flux at each point and the difference variable between them, PI−APC starts to operate its loops.

With monitored PIs and other equipment variables, the current status of the etch process is estimated with PI−VM model in process control loop. In this case, the difference variable of mask height, $\Delta_r H_{mask}(t)$ is estimated at time $t$. To get the degree of control action with CV, the difference of the PI, ion energy flux variable, $\Delta_r \Gamma_E$, needed etch rate of the mask is calculated with several time step, $k$ of given system sampling time, $\Delta t$,

$$\Delta_r ER_{mask,set} = \frac{\Delta_r H_{mask}(t)}{k\Delta t} \tag{5.1}$$

where, $\Delta_r ER_{mask,set}$ is the set value of the difference variable of mask etch rate with counter directive action for improving etch uniformity. The degree of the time step, $k$ is considered for marginal time for progression of surface reaction accumulation. If $k$ is too short, the dual−loop controller become unstable due to requirement of excessive control action over given operation window. In this system, stable control with $k \geq 10$ is achieved.

After the set−point of process variable is determined, the set−point of PI variable is calculated to get the next operation degree of MV in plasma control loop. In this step, invers function of PI−VM model is used,

$$PI_{set} = \Delta\Gamma_{E,set} = VM^{-1}\left(\Delta_r ER_{mask,set}\right) \tag{5.2}$$

where, $PI_{set}$ is the set−point of PI variable to get the improved process uniformity at next step. In the plasma control loop, model predictive control (MPC) algorithm is adapted. MPC is an advanced control algorithm that predicts future moves of the output and calculate optimized control moves [00]. Figure 5.3 shows that the basic structure of MPC is composed with predictor and optimizer including cost function and constraints. Predictor contains an internal model that describes dynamics between input and output. Optimizer calculates the control moves to minimize quadratic objective function which quantifies the importance of output error and input variation. Internal model used in this study will be treated in Chapter 5.2 and determination of objective function with output error and weighting will be handled in Chapter 5.3. In any case, the set−value of the MV, edge ring power, to adjust PI variable is updated with forwarding it to RF power supply.

$$P_{edge,set} = P_{edge}\left(t\right) + \Delta P_{edge} \tag{5.3}$$

Final sampling time for process uniformity control is determined by tangled double loop between process and plasma controller, while control time of each loop is different with the ratio of k. In other words, during updating the set−value of the process variable with 1 cycle, the set−value of the MV is updated with k cycles. This means that plasma is controlled within constraints and maintained to given set−value $k$ times faster than process be. This makes plasma process operate stable operation with drift disturbance.

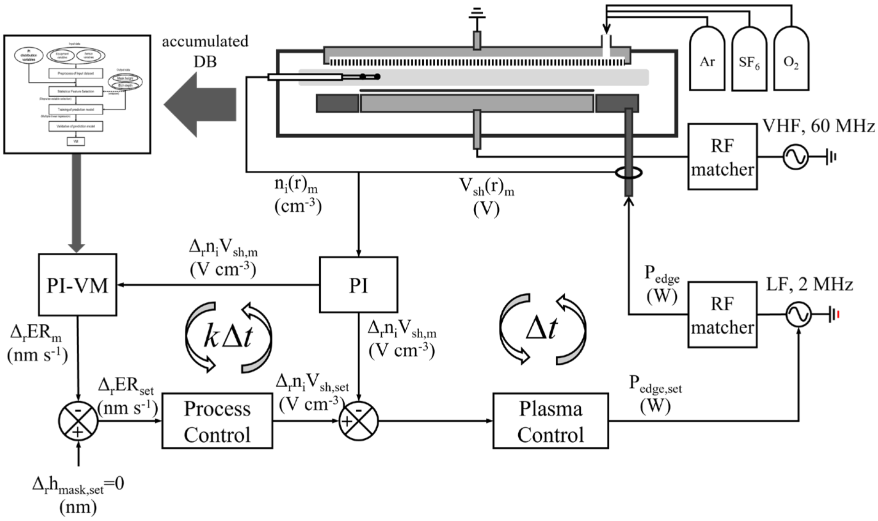


Figure 5.2. Control diagram consisting of dual loop with equipment–plasma control and plasma–process control loops with capacitively coupled etcher with RF powered edge ring.

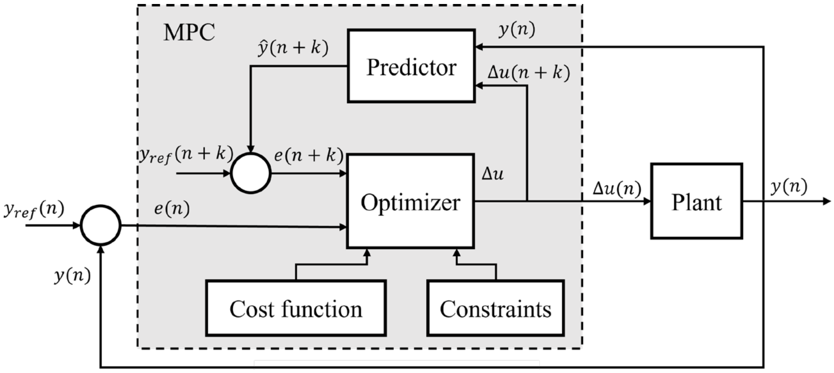


Figure 5.3. Model predictive control algorithm composed with predictor and optimizer.

## 5.2. Open-Loop Data-Driven Plasma Dynamics Control Model

Plasma dynamic model for equipment-plasma control loop can be developed from open-loop control data, as shown in Figure 5.4 for the difference of ion energy flux between two different radial position, $\Delta_r\Gamma_E$ with RF power variation on edge ring. From the developed theoretical steady-state model in chapter 3.3, the control gain was estimated about $-5.15\times10^{11}$ Vcm$^{-3}$W$^{-1}$ with zero difference at about 30 W RF power. For a linear operation of RF powered edge ring on edge uniformity control with bi-directional action, an intersection point with zero difference should be included in MV operation window. As show in Figure 5.5, linear correlation between MV and CV variation within 90 W RF edge ring RF power is confirmed similar with Figure 3. 13. Also, the model gain of about $-3.27\times10^{11}$ Vcm$^{-3}$W$^{-1}$ from open-loop test data is similar with the gain from theoretical model.

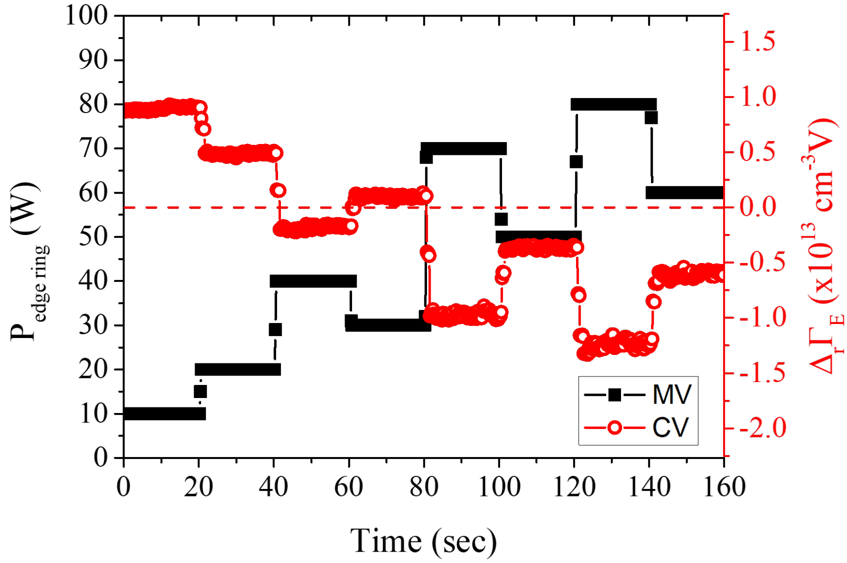


Figure 5.4. Time transition of MV ($P_{edge\ ring}$) and CV ($\Delta_r\Gamma_E$) operation in open-loop test experiment.

With open-loop test data, control dynamic model can be developed with first-order transfer function in Equation (5.4). The general first-order transfer function is given with the steady-stat gain, $G$ and the time constant, $\tau$. In this study, the dynamic plasma model for the difference variable of ion energy flux to edge ring RF power has $-3.27\times10^{11}$ $\mathrm{Vcm^{-3}W^{-1}}$ gain and 2.02 sec time constant. It means that after 2.02 sec of MV operation, CV value reaches the set-value without delay within sampling time. Note that, although the dynamic model was developed without time delay, it can be existed but cannot be recognized with longer sampling time about 0.2 sec. As the plasma dynamic control model, first-order transfer function in Equation (5.4) was used as a predictor in MPC algorithm to predict change of the difference value in ion energy flux by manipulating RF power on the edge ring.

$$\begin{aligned}\Delta\left(\Delta_r\Gamma_E\right) &= \frac{G}{\tau s+1}\Delta P_{edg} \\ &= \frac{-3.27\times10^{11}}{2.02s+1}\Delta P_{edg}\end{aligned} \tag{5.4}$$

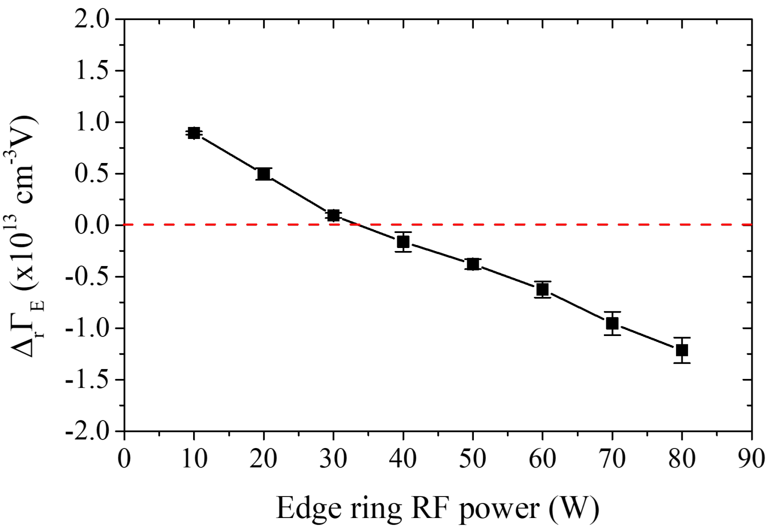


**Figure 5.5.** Linear relation between MV ($P_{edge\ ring}$) and CV($\Delta_r\Gamma_E$) values with negative gain from re-arranged data with averaged value of each variation of conditions.

## 5.3. Closed−Loop PI−APC Results of Mask Height Uniformity

With PI−APC system in Figure 5.2 and developed plasma dynamics model, the closed−loop controller operates to maintain mask height uniformity represented by the difference of mask height at the radial position of 120 and 145 mm on wafer. Although control target is the difference variable of mask height, etch depth with the same process was also monitored with the developed PI−VM model in chapter 4.2. Operation results of PI−APC in short process time is shown in Figure 5.6 within 80 sec. PI−APC algorithm started at 10 sec after starting of the process due to distinct control action with worsen uniformity environment. At the time when PI−APC started, the difference of mask height between two edge position is about 2.5 nm. Just after PI−APC was involved in the process, mask uniformity was exacerbated during about 5 sec. This was due to not enough manipulation of edge ring power degree in 5 sec to pass the operation regime of positive feedback, although controller continuously increased edge ring power. After 15 sec in process time, the difference value of the mask height started to be decreased toward zero difference value. At about 25 sec of the process time, the mask uniformity was satisfied with process control target of zero difference value, while the controller could not change the control direction to inverse trend. This is because there was still the error between the set and the monitoring value of the $\Delta_r\Gamma_E$ , so the adjustment of the edge ring power to compensate for this error even if the mask uniformity was achieved in the process control loop. In other words, the weight of the error for CV was less than that of the change for MV in the plasma control loop. This control operation characteristics can be improved by determining weighting values in MPC algorithm. Nevertheless, the difference value of the mask height was converged to zero value with attenuation vibration behavior, as the PI−APC continuously operated in process.

Figure 5.7 shows that there is no difference in mask height at the end of the process as a result of the PI-APC continuously operating for a given process time about 280 sec. Although the stabilization was slow, the difference of the remain mask height almost zero after the process time about 100 sec, and the oscillation of the PI variable also was reduced. The amplitude of the oscillation of the variable was larger for the RF power on the edge ring (MV) than for the difference of the ion energy flux variable (CV) because the weighting coefficients for the change of MV was set to relatively larger than that for the error of CV. This is treated in following section about control optimization.

The variation of the MV until the end of the process in Figure 5.6, the MV value slightly increased by about 4.7 W for 180 sec after the stabilization time at 100 sec. This means that although the PI-APC developed in this study did not have the model for compensating drift effect of the equipment, the real-time process control model worked to compensate for a subtle drift with unknown cause. From the operation result of the PI-APC in which the RF power of the edge ring was slightly increased, it can be inferred that the drift which made the etch rate at the wafer edge slightly reduced occur under the experimental conditions of this equipment. While an exact cause analysis of this drift was not performed, it can be inferred that there was a change in wall condition as the operation time of the equipment accumulated.

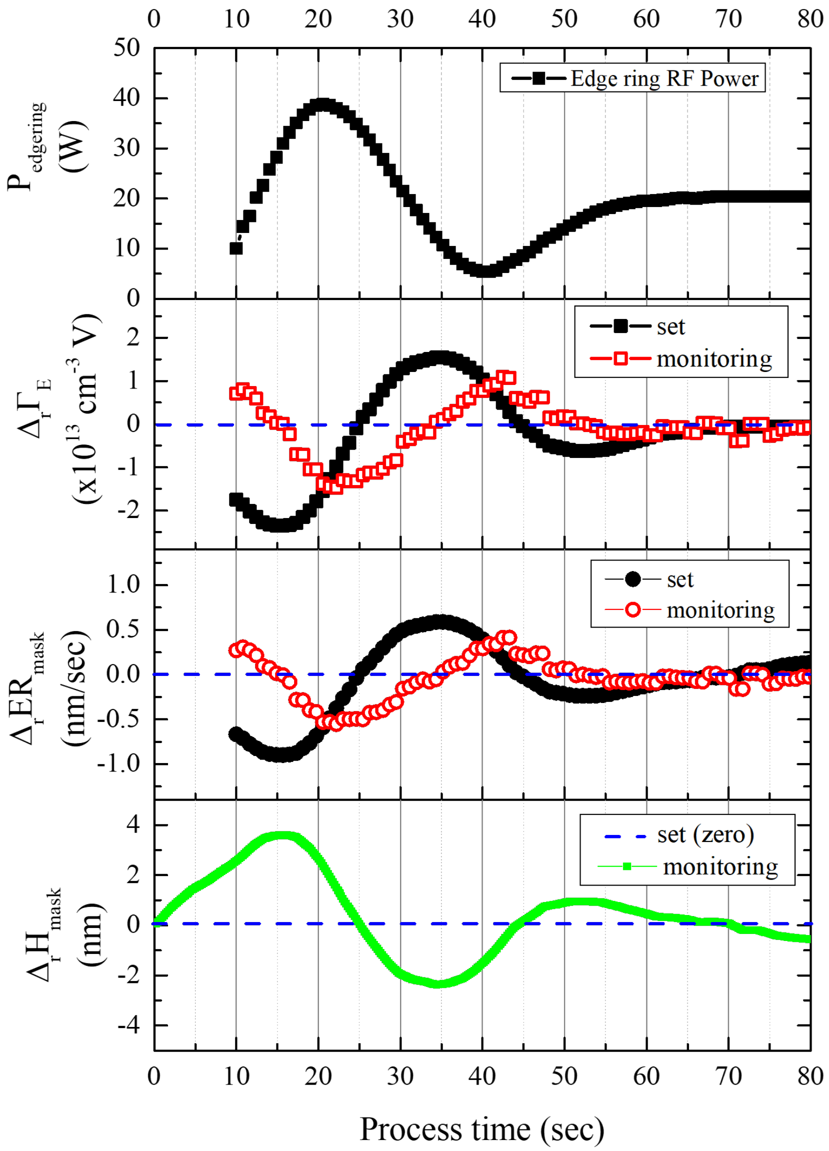


Figure 5.6. Short time closed−loop control results during process time of 80 sec with controlled difference variable of ion energy flux and mask etch rate resulting in controlled difference of mask height by manipulated edge ring RF power.

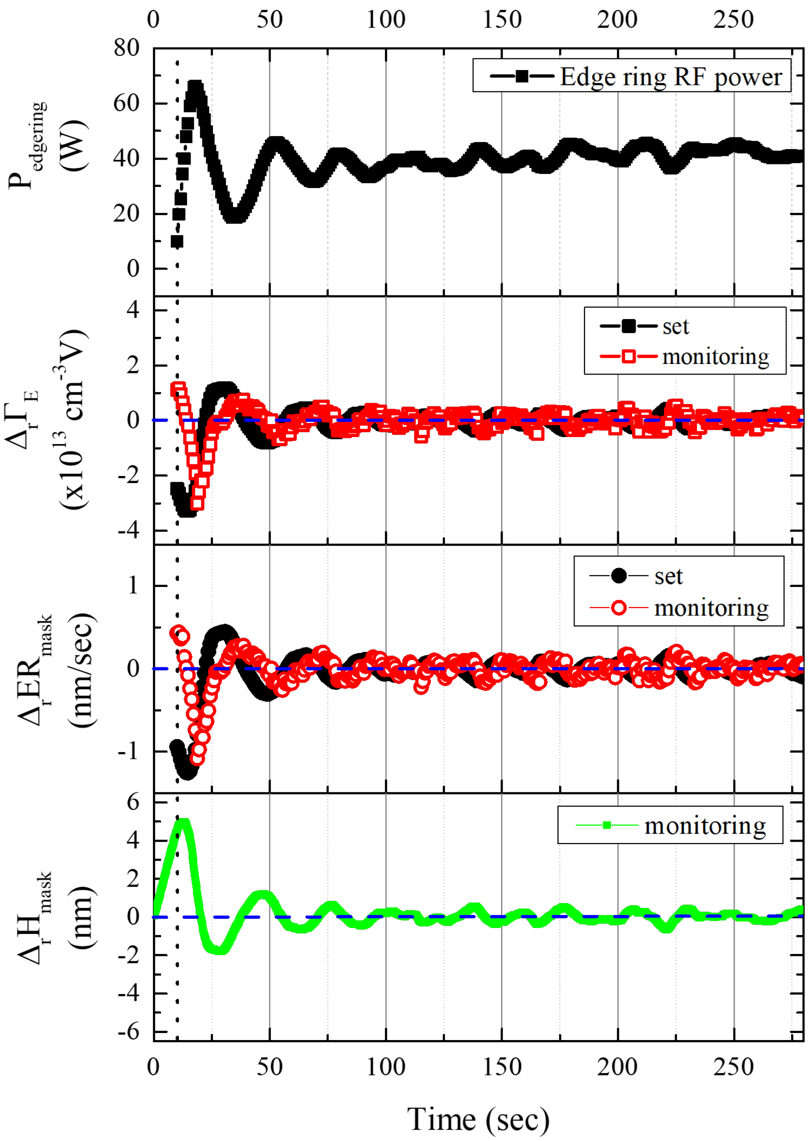


Figure 5.7. Full time closed-loop control results during process time of 280 sec with controlled difference variable of ion energy flux and mask etch rate resulting in controlled difference of mask height by manipulated edge ring RF power.

As the PI−APC for controlling the difference of the mask height in wafer edge is operated in real−time, the difference value of not only the mask height but also the etch depth of the Si mold target is controlled to near zero value. Variation of the predicted remain height of the $SiO_2$ mask and etch depth of the Si mold target during process time with PI−APC operation is shown in Figure 5.8 (a) and (b). Compared with the result of process operation with PI−APC, Figure 5.9 (a) and (b) also shows the time series process results, remain mask height and mold etch depth.

With PI−APC operation, both edge uniformity (difference value between 120 and 145 mm positions) of the $SiO_2$ remain mask height and Si mold etch depth had obtained with similar results, although the process control target was set to only mask height variable. It means that trench pattern Si profile etch uniformity can be improved just by controlling mask etch uniformity. Due to a common control variable with PI of the ion energy flux, the mold etch depth was also controlled.

Without PI−APC operation, both etch rate of $SiO_2$ mask and Si mold at outer position at 145 mm is lower than that at 120 mm. This process condition was maintained during all process time resulting in large differences in remain mask height and mold etch depth about 148 nm and 64 nm at each with prediction model results.

Figure 5.10 shows the process results in real with the same operation of Figure 5.8. As predicted in virtual operation with process prediction model, the difference value of mask remain height and mold etch depth between 120 and 145 mm was reduced from about 80 nm and 77 nm without PI−APC to 4 nm and 43 nm with PI−APC. Therefore, it is validated that the developed PI−APC consisting of the plasma and process control loops intertwined in cascade structure can improve the process uniformity by using the difference value of PI between two different position as inter−parameter.

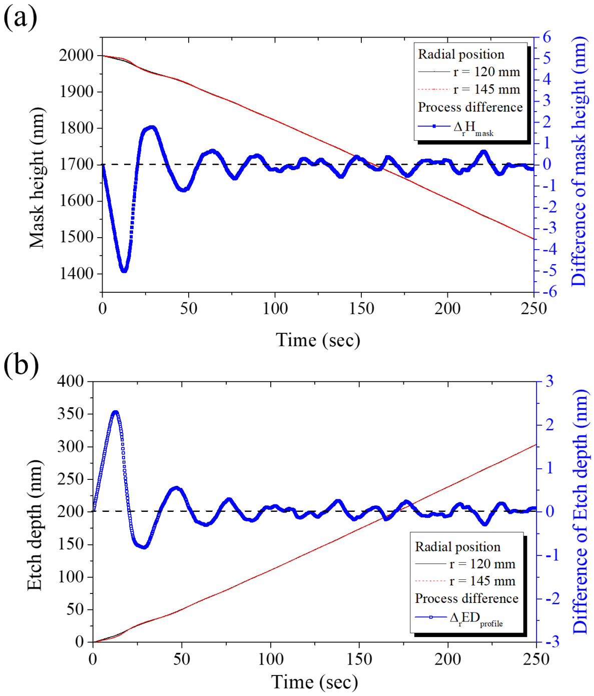


Figure 5.8. With PI−APC for edge uniformity of mask height, time transition of (a) the $SiO_2$ mask height and (b) the Si mold etch depth at two radial position and its difference.

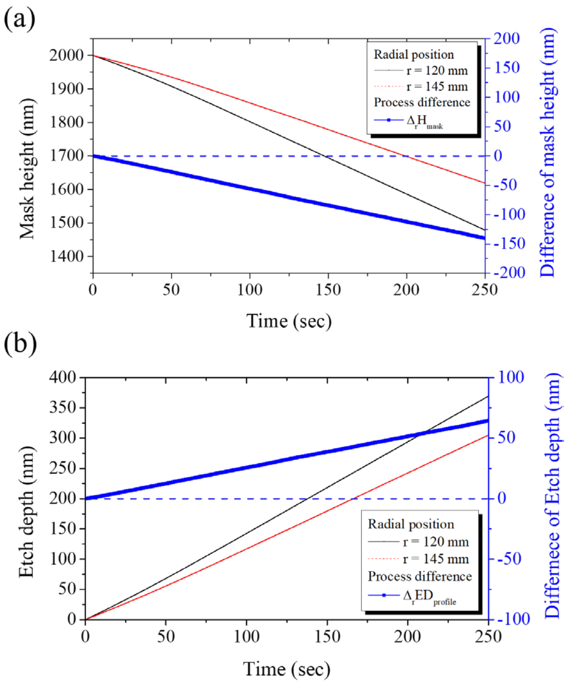


Figure 5.9. Without PI−APC for edge uniformity of mask height, time transition of (a) the $SiO_2$ mask height and (b) the Si mold etch depth at two radial position and its difference.

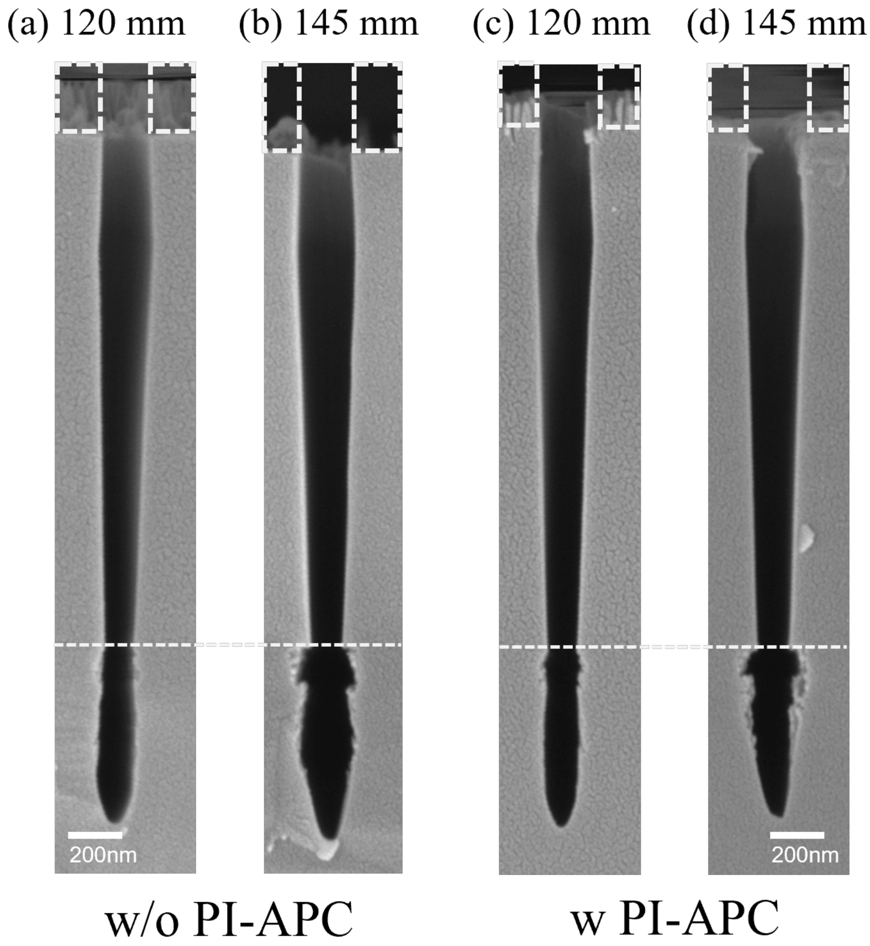


Figure 5.10. Process results of SEM images without PI−APC operation at (a) 120 mm and (b) 145 mm and improved process edge uniformity with applying PI−APC at (c) 120 mm and (d) 145 mm.

## 5.4. Optimization of Developed Controller

As mentioned in previous section, performance of the developed controller has dependency with weighting coefficients in MPC control algorithm [44]. In Figure 5.3, MPC controller has the predictor including internal model and the optimizer defining control action. For generally used quadratic objective function, $J$ is expressed as [13]

$$J\left(z_k\right)=\sum_{i=1}^{P} e_y^T\left(k+i\right)Qe_y\left(k+i\right)+\sum_{i=1}^{M} u'^T_y\left(k+i\right)Ru'\left(k+i\right) \tag{5.5}$$

where, Q is the weighting for error for controlled variable, $e_y$, R is the weighting for change of manipulated variable, $u'$, P is the prediction horizon and M is control horizon. The error of controlled variable is calculated with,

$$\begin{aligned} e_y\left(k+i\right) &= y_{set}\left(k+i\right)-\hat{y}\left(k+i\right) \\ &= y_{set}\left(k+i\right)-\sum_{j=1}^{i} S_j u'\left(k+i-j\right) \\ &\quad +\sum_{j=i+1}^{n-1} S_j u'\left(k+i-j\right)+S_n u'\left(k+i-n\right) \end{aligned} \tag{5.6}$$

where, $y_{set}$ is the set−point of controlled variable, $\hat{y}$ is the trajectory of controlled variable, $S_i$ is the step−response function based on the linear control model.

As a performance index of controller, the integral of the squared error (ISE) value can be used.

$$ISE=\int_0^T e^2\left(t\right)dt \tag{5.7}$$

Assuming that the same transfer function model obtained from open−loop data previously described in Equation (5.4) and in−real system, parameter study for the dependency of the Q and R weightings by simulating set−point tracking test. Figure 5.11 shows the simulation result. According to this result, the best performance condition considering only ISE value is at highest Q and lowest R like highest Q/R ratio. This means that the more weight to the error of the CV than to the change of the MV, the more quickly stabilized within certain time. Figure 5.12 also shows the simulation results of the plasma control depending on Q/R ratio. If Q/R ratio is set to a value of 10, CV quickly reaches to a given set value but with moving excessively having large amplitude. Unlikely, if Q/R ratio is set to a value of 0.1, control action is sluggish nevertheless large difference from the given set value at initial time with stabilizing slowly but with small amplitude oscillation. Therefore, in optimization procedure, there is trade−off between stabilizing time for control speed and oscillating amplitude for a risk of exceeding operation constraints.

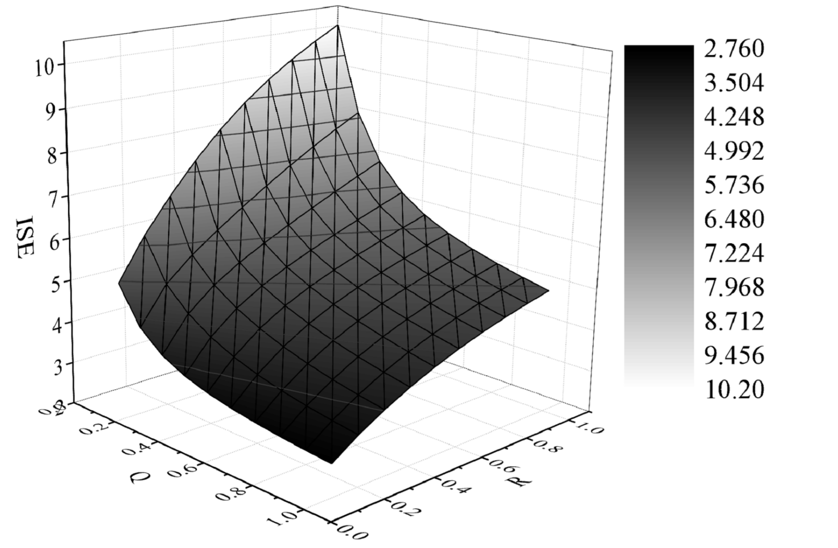


**Figure 5.11. Contour surface of integral of the square error (ISE) resulted from simulation of set−point tracking test with linearized Q and R combination.**

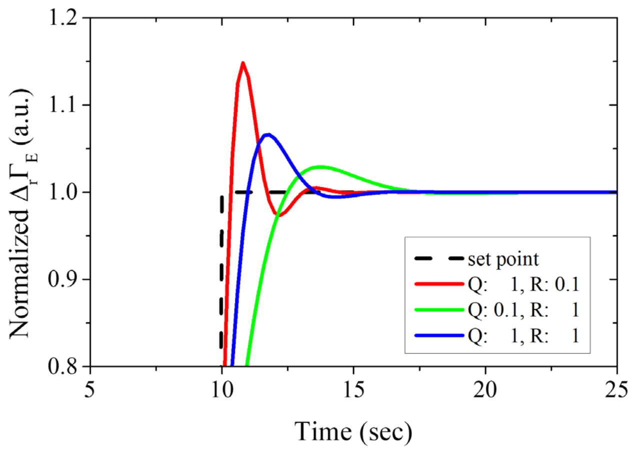


**Figure 5.12. Simulation of closed-loop control test depending on the Q and R combination.**

Following the simulation results, the developed PI-APC is adjusted to improve control performance in reference of performance index. Figure 5.13 shows different control movements of PI depending on the Q/R ratio set in the MPC algorithm of PI-APC. Unlike to the previous simulation result, the best performance with lowest performance index values of IAE and ITEA is achieved with the ratio value of 1 (Table 5.1). With Q/R ratio of 0.025, PI variable followed set value with about 2 sec of delay time, during which the performance index could be increased. In case of the Q/R ratio with the value of 1, excepting initial time about 5 sec, PI variable quickly followed tightly with set value. However, with highest value of Q/R ratio about 40, control action was unstable with excessively moving to reach the given set value within sampling time. As previously described, there was failure to find stable state given trade-off relation.

**Table 5.1. Performance index (IAE, ITAE) depending on Q/R ratio of MPC algorithm in PI-APC.**

| Q/R ratio | IAE | ITAE |
|---|---|---|
| 0.025 | $1.05\times10^{13}$ | $1.22\times10^{14}$ |
| 1 | $8.58\times10^{12}$ | $1.01\times10^{14}$ |
| 4 | $4.20\times10^{13}$ | $9.78\times10^{14}$ |

(a) Q/R = 0.025

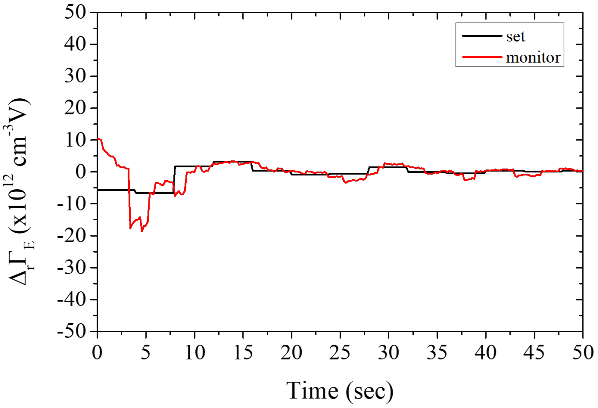


(b) Q/R = 1

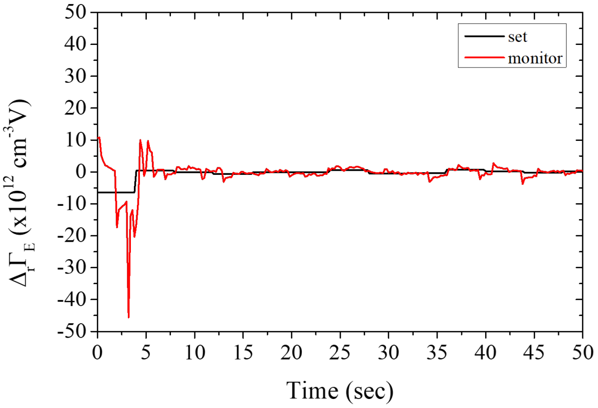


(c) Q/R = 40

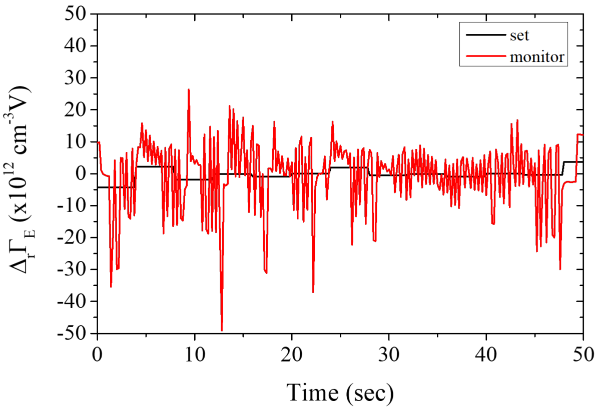


Figure 5.13. Plasma control result of the difference value of ion energy flux during process time of 50 sec with Q/R ratio of (a) 0.025, (b) 1 and (c) 40.

Different optimization value of the Q/R ratio between control simulation and in−real control result could be from different gain value between the control model and in−real condition. It is simulated with introducing multiplier parameter, $x$ to a gain in the used control model and assumed to occur mismatched gain condition between used control model and in−real situation. Figure 5.14 shows simulated results of set−point tracking test in Q/R parameter study. With increasing difference in gain value between in control model and real situation, the best performance condition moves from highest Q/R value to certain value about 1.

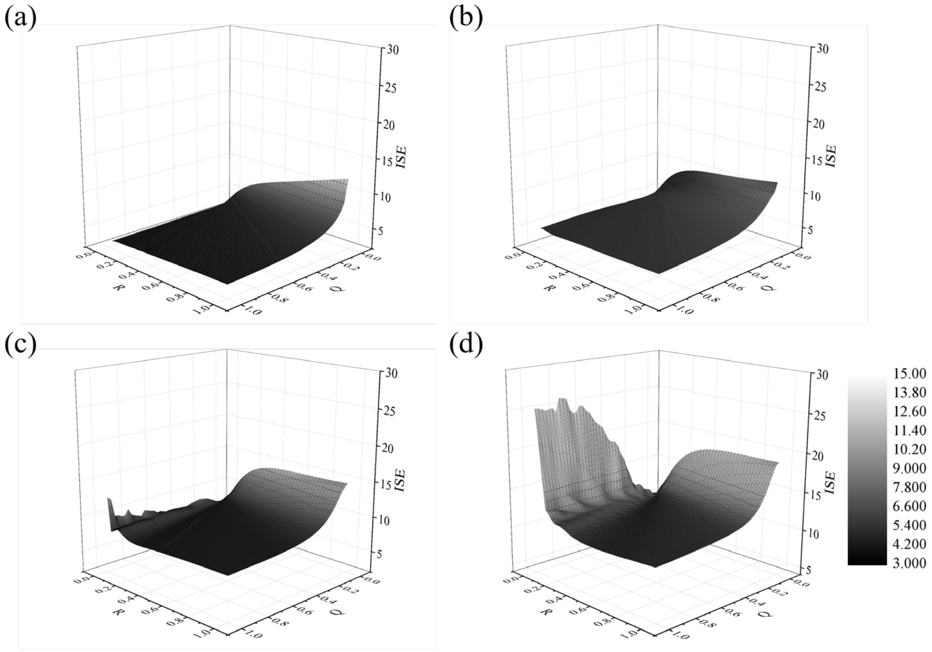


Figure 5.14. Contour surface of integral of the square error (ISE) resulted from simulation of set−point tracking test with linearized Q and R combination in case with mismatched model between control and plant for multiple about (a) same, (b) 1.5, (c) 2, and (d) 2.5.

For improving control performance, the sampling time ratio, $k$ between two control loops can be adjusted. It is a distinct parameter from cascade structure of the PI−APC. $k$ is introduced by considering process reaction rate relatively shorter than sampling time in plasma control loop. Set value of the process rate linearly relating set value of the PI is determined by $k\Delta t$ for a given set value of length scale, such as mask height and etch depth. For example, for a current predicted difference of mask height in time, $t$, $\Delta_r H_{mask}(t)$, required mask etch rate which is set value to compensate that difference value is calculated with below.

$$\Delta_r ER_{mask,set}\left(t+k\Delta t\right)=\frac{\Delta_r H_{mask}\left(t\right)}{k\Delta t} \tag{5.8}$$

where, $\Delta_r$ means difference between two positions representing uniformity, $ER$ is etch rate, $H$ is etch depth or remain height, $\Delta t$ is the sampling time of plasma control loop.

Figure 5.15 shows control results of PI−APC to maintain zero difference of the mask height depending on value of $k$. The Q/R ratio is constant to 1. As the relation of the set value of the process control loop, the difference of the remain mask height is quickly reached to a zero set value with small value of $k$. However, an amplitude of oscillation of the process also increases resulting in large error between set value in oscillating duration at initial time. Figure 5.16 shows control movement of the process with shorter time in initial 50 sec operation. With increasing value of $k$, oscillating amplitude decreases but oscillating time increases. According to the performance index meaning accumulated error during full process time, the best performance is achieved with the set of $k=20$.

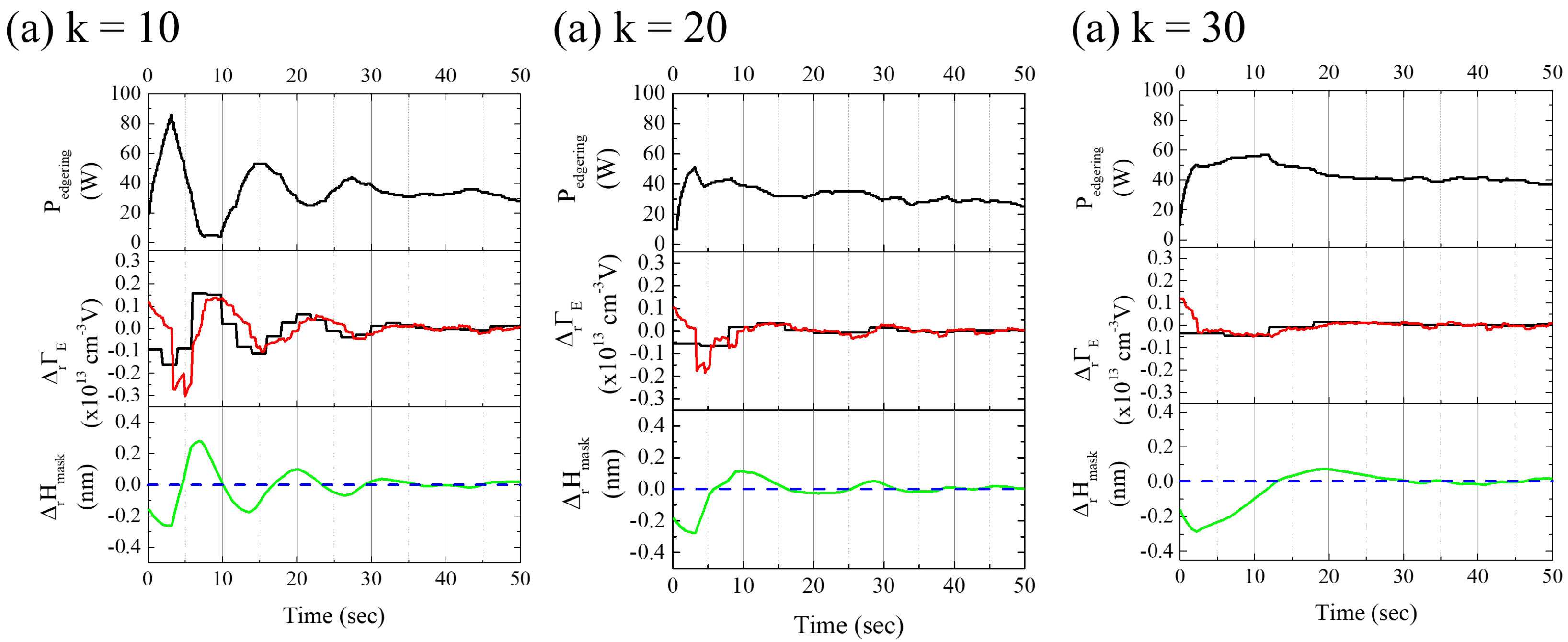


Figure 5.15. Process uniformity control results with the process prediction window value of (a) k = 10 shows aggressive control due to required large PI variation in short time, (b) k = 20 shows stable controlled mask uniformity with initial oscillation within 20 sec of process time, (c) k = 30 shows sluggish controlled with long stable time within 30 sec of process time.

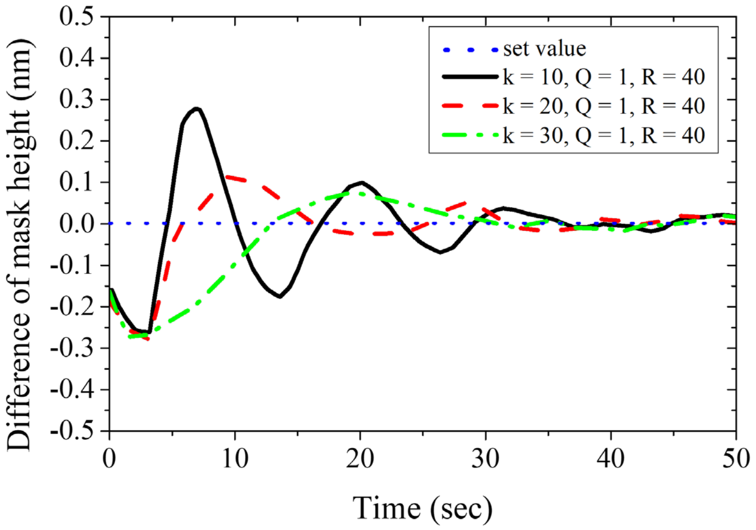


Figure 5.16. Oscillation of the uniformity of the process result (mask height) at initial control time depending on the process prediction window length, k.

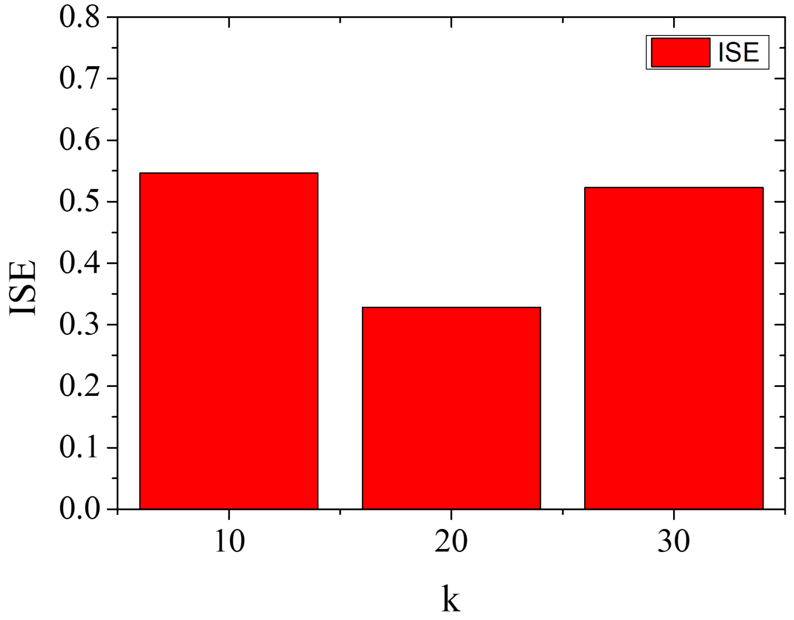


Figure 5.17. Assessment of control performance with ISE value depending on the process prediction window, k shows optimal control condition with k = 20.

# Chapter 6. Conclusion

For the real-time control of the etching process uniformity in the semiconductor manufacturing, the advanced process control (APC) methodology was systematically established based on the plasma information (PI) variables. In accordance with the control objective of process uniformity in wafer edge region, the edge ring surrounding the wafer electrode was adopted to make change on plasma distribution with actively applied RF power. The plasma power balance and the equivalent circuit model allow the determination of the manipulating characteristics of operation window and controllable region with efficient design of experiments (DOE). Through the consideration of the basic characteristics on the plasma density and sheath potential distribution correlated with the process uniformity in plasma-assisted process equipment, the ion energy flux variable with radial slope formation was featured as the principal parameter to explain the etching of $SiO_2$ mask and Si mold. Until now, the control target for the plasma distribution and process uniformity have been represented with just several positional points and without correlation between radial directional distribution of plasma and process uniformity. However, unlike the previous studies regarding the process uniformity control, this study presents the radial slope formation of the controlled variable for representing edge plasma distribution determining etch process uniformity. This approach makes the uniformity controller more easily constructed with the single-input single-output (SISO) than with the multiple-input multiple-output (MIMO) system requiring identification of correlations between variables with many times. Ultimately, APC has a dual-loop structure, also known as a cascade, intertwining two SISO control loops each for equipment-plasma and plasma-process with different sampling time due to that the process results such as etch depth and mask height appears after a certain period of the process time. Here, the PI is the significant parameter to link the plasma and process control with being controlled by external knob and determining etch rate in each loop. From this cascade structure, there are several tuning parameters to determine the control performance and stability, which are the Q/R ratio representing response performance about control action in the plasma control loop and the k meaning the prediction window of the etch depth in the process control loop. In cascade control structure, too large k makes sluggish process control response for the controlled PI and too small k results in control instability due to similar or smaller prediction window for the plasma control. With consideration of the mismatch between control and plant model, the optimized Q/R ratio value is determined with specific value depending on the system. For the more improved performance and stability, gain scheduling and adaptive model predictive control algorithm can be adopted to transition of the gain depending on operation regimes. This thesis shows that the PI–APC for the plasma–enhanced process not only enables real–time process control based on plasma phenomenology, but also can suggests the guide for tuning upcoming process run and maintenance. With the accumulated time series database of PI–APC including the plasma information governing process results, the dynamic characteristics of the process and equipment environment during previous process run, such as the drift analysis, can give insight to develop advanced run–to–run (R2R) control, tool–to–tool matching (TTTM), and next generation plasma equipment.

# Bibliography

[1] J. Moyne, Introduction to and Practical Application of APC: A Tutorial. In Proceedings of the Advanced Process Control Conference XXVII, Phoenix, AZ, USA, 17–20 October 2016.

[2] J. Moyne, J. Iskandar, *Processes* **5**, 3 (2017).

[3] J. Moyne, E. Del Castillo, A. Hurwitz, *Run–to–Run Control in Semiconductor Manufacturing* (CRC Press, Boca Raton, FL, USA, 2000).

[4] Fan–Tien Cheng, Industry 4.1 (IEEE Press, NJ, USA, 2022).

[5] K. Liu, YQ. Chen, T. Zhang, S. tian, X. Zhang, *ISA Transactions* **83** (2018).

[6] Demetre J. Economou, *Thin Solid Films* **365** (2000).

[7] S. Lynn, N. MacGearailt, J. V. Ringwood, *Journal of Process Control* **22** (2012).

[8] P. Kang, H. Lee, S. Cho, D. Kim, J. Park, C.–K. Park, S. Doh, *Expert Systems with Applications* **36** (2009).

[9] P. Kang, D. Kim, H. Lee, S. Doh, S. Cho, *Expert Systems with Applications* **38** (2011).

[10] Paul–Arthur Dreyfus, et al., *Journal of Manufacturing Systems* **63** (2022).

[11] S. Park, S. Jeong, Y. Jang, S. Ryu, H.–J. Roh, G.–H. Kim, *IEEE Transactions on Semiconductor Manufacturing* **28**, 3 (2015).

[12] S. Ryu, *"Development of Plasma Information Based Advanced Process Controller (PI–APC) for Plasma Etch Processes"*, Seoul National University, Ph.D Thesis, 2021.

[13] D. E. Seborg, T. F. Edgar, D. A. Mellichamp, F. J. Doyle III, *Process Dynamics and Control (3rd ed.)* (John Wiley & Sons, USA, 2011)

[14] N. Negishi, M. Miyake, K. Yokogawa, M. Oyama, T. kanekiyo, M/. Izawa, J. Vac. Sci. Technol. B **35** (2017)

[15] M. Miyake, N. Negishi, M. Izawa, K. Yokogawa, M. Oyama, T. Kanekiyo, *Japanese Journal of Applied Physics* **48** (2009).

[16] J.–K. Lee, I.–Y. Jang, S.–H. Lee, C.–K. Kim, S. H. Moon, *Journal of The Electrochemical Society* **157** (3) (2010).

[17] D. Hayashi, J. Nakai, M. Minami, T. Kamimoto, and Y. Deguchi*, J. Phys. D Appl. Phys.* **52** (2019).

[18] D. Hayashi, Y. Sakaguchi, M. Minami, *AIP Advances* **11** (2021).

[19] Y. Deguchi, T. Kamimoto, Z. Z. Wang, J. J. Yan, J. P. Liu, H. Watanabe, R. Kurose, *Appl. Therm. Eng.* **73** (2014).

[20] Milenin, A. P., Boullart, W., Quli, F., & Wen, Y. *Japanese Journal of Applied Physics* **53**(3S2), (2014).

[21] J. S. Kim, M. Y. Hur, H. J. Kim, H. J. Lee, *Journal of Applied Physics* **126** (2019).

[22] Wang, X., Lee, H., Nam, S. K., Kushner, M. *Journal of Vacuum Society and Technology A* **39** (6), (2021).

[23] I. Sawada, P. L. G. Ventzek, B. Lane, T. Ohshita, et al., Japanese *Journal of Applied Physcis* **53** (2014).

[24] M. A. Lieberman, A. J. Lichtenberg, E. Kawamura, T. Mussenbrock, R. P. Brinkmann, *Physics of Plasmas* **15** (2008).

[25] K. Zhao, D. Q. Wen, Y. X. Liu, M. A. Lieberman, D. J. Economou, Y.-N. Wang, *Physical review letters* **122** (2019).

[26] J. K. Liu, E. Kawamura, M. A. Liberman, Y.-N. Wang, *Physics of Plasmas* **29** (2022).

[27] M. A. Lieberman, *Principles of plasma discharges and materials processing* (John Wiley & Sons, NJ, 2005)

[28] P. Chabert and N. St. J. Braithwaite, *Physics of Radio-Frequency Plasmas* (Cambridge university press, UK, 2011)

[29] Myung-Sun Choi, "Development of Equivalent Circuit Model for Very High Frequency Driven Capacitively Coupled Plasmas", Seoul National University, Ph.D Thesis, 2014.

[30] K. Kohler, et al., *J. Appl. Phys.* **57** (1985).

[31] Yunchang Jang, *"Plasma Information Variables Based on Ion Dynamics in Collisional RF Sheath for Etching Profile Monitoring"*, Seoul National University, Ph.D Thesis, 2020.

[32] J. W. Coburn, M. Chen, *Journal of Applied Physics* **51** (1980).

[33] D. V. Lopaeve, A. V. Volynets, S. M. Zyryanov, A. I. Zotovich, A. T. Rakhimov, *Journal of Physics D: Applied Physics* **50** (2017).

[34] P. Chabert, J. L. Raimbault, J. M. Rax, et al., *Physics of Plasmas* **11** (2004).

[35] X.-M. Zhu, W.-C. Chen, S. Zhang, Z.-G. Guo, D.-W. Hu, Y.-K. Pu, *Journal of Physics D: Applied Physics* **40** (2007).

[36] S. W. Butler, K. J. McLaughlin, T. F. Edgar, I. Trachtenberg, *Journal of The Electrochemical Society* **138** (1991).

[37] J. Koo, D. Ha, D. Park, H.-J. Roh, S. Ryu, G.-H. Kim, K. H. Baek, C. Han, *Computers & Chemical Engineering* **100** 8 (2017).

[38] Y. Jang, H.−J. Roh, S. Park, S. Jeong, S. Ryu, J.−W. Kwon, N.−K. Kim, G. H. Kim, *Current Applied Physics* **19** 10 (2019).
[39] J. Song, M. Lee, S. Ryu, Y. Jang, S. Park, G. H. Kim, *Current Applied Physics* **45** (2022).
[40] M. Farres, S. Platikanov, S. Tsakovski, R. Tauler, *J. Chemom* **29** (2015).
[41] J. Ding, N. Hershkowitz, *Applied Physics Letters* **68** (1996).
[42] L. Stafford, J. Margot, M. Chaker, et al., *Applied Physics Letters* **87** (2005).
[43] M. A. Blauw, E. van der Drift, G. Marcos, et al., Journal of Applied Physics **94** (2013).
[44] M. Morai, J. H. Lee, Computers & Chemical Engineering **23** (1999).

# 국문초록


플라즈마를 이용하는 반도체 및 디스플레이 제조 공정의 안정적인 공정 수행 및 수율 관리를 위하여 고급 공정 제어 (APC) 가 적용된다. APC는 주어진 제어 대상의 목표치와 모니터링되는 제어 인자의 현재 상태 값 간의 이격 차이를 인지한 후, 이를 보상하기 위해 필요한 조절 인자의 변화량을 계산하여 해당 인자 변화를 자동으로 장비에 적용한다. 플라즈마를 이용하는 반도체 식각 공정의 궁극적인 제어 대상은 식각 깊이와 같은 공정의 결과값이며, 이는 플라즈마 인자와 웨이퍼 표면에서의 반응률에 의해 결정되므로, 해당 현상학을 기반으로 구성된 모델을 활용한 플라즈마 인자의 조절이 요구된다. 또한 이러한 플라즈마 인자의 조절은 플라즈마가 생성되는 반도체 장비의 운전 인자에 의해 결정되므로 장비-플라즈마 제어 루프와 플라즈마-공정 제어 루프가 연동된 제어 구조로써 플라즈마 이용 공정에 대한 고급 공정 제어기인 PI-APC가 구성된다.

PI-APC 시스템은 제어의 목표가 되는 대상의 특성에 부합하는 플라즈마 정보 인자와 이의 모니터링을 위한 센서 및 제어를 위한 적합한 조절 인자의 설정이 요구된다. 본 연구에서의 공정 제어 목표는 웨이퍼 가장자리 영역의 산포를 의미하는 웨이퍼 반경 방향 120 및 145 mm의 2개 지점에서의 Si 식각 깊이의 차이값으로 정의된다. 이에 따라, CCP 식각 장비 내에서의 플라즈마 밀도 및 쉬스 포텐셜 분포 모니터링을 위한 2개의 탐침 배열과 하부 전극에 연결된 VI 센서를 구성하였다. 플라즈마 분포 특성 제어를 위한 조절 인자로써 엣지링 부품에 인가되는 RF 전력량을 이용하였다. 엣지링에 인가되는 RF 주파수가 증가할수록 웨이퍼 영역 내에 영향을 미치는 유효 거리가 증가함을 확인하였으며, 웨이퍼 가장자리 영역 30 mm 이내에서의 분포 기울기 조절에 적합한 2 MHz 주파수가 사용되었다.

대상 공정으로 선정된 트렌치 패턴을 가지는 산화 실리콘 ($SiO_2$) 마스크를 가지는 실리콘 (Si) 타겟에 대한 공정 모델을 플라즈마 정보 인자를 활용한 가상 계측 기술 (PI-VM)을 활용하여 개발하였고, 이를 PI-APC의 공정 제어 루프 내 공정 결과 예측 모델로써 사용한다. 현상학 기반으로 개발된 PI 인자를 활용한 PI-VM 모델은 여러 설명 인자에 대한 선형 조합으로 구성되기 때문에 PI-APC 시스템에서 복잡한 연산에 대한 부담을 경감시키며 공정 결과 예측에 활용된다. 본 연구의 대상인

$SiO_2$ 마스크 및 Si 몰드 식각의 주요 기여종으로써 공통적으로 이온 에너지 플럭스의 PI 인자가 선택되었으며, 두번째 기여 인자로써 각각 플로오린 (F) 및 산소 (O) 라디칼 밀도가 마스크 및 몰드 식각 반응에 기여함을 확인하였다. 산화 실리콘 물질에 대해서 F 라디칼은 표면 활성화 및 화학적 식각 반응으로 식각을 증진시키며, O 라디칼은 실리콘 표면에서 보호막을 형성하여 이온에 의한 식각을 방해할 수 있다. 선택 중요도 상 두 타겟 물질의 식각에 가장 큰 기여도를 가지는 이온 에너지 플럭스를 플라즈마 제어 루프의 제어 인자 및 공정 제어 루프의 조절 인자로써 사용한다.

앞서 개발한 센서 구성, PI 인자 및 PI-VM 모델들을 연동하여 모델 예측 제어 (MPC) 알고리즘 기반의 다단 제어 구조의 PI-APC가 개발되었다. MPC 알고리즘 내 목적 함수 내에서 CV 차이에 대한 가중치인 Q 계수와 MV 변화량에 대한 가중치인 R 계수의 비율인 Q/R 값에 따라 제어기의 안정성 및 전체 시간동안 목표 값과의 차이로 결정되는 성능이 결정되었다. 또한, 다단 제어 구조 특성으로부터 공정 제어 루프의 샘플링 시간 설정에 따라 제어 안정화 시간이 결정되었다. 이러한 특성은 사용된 플라즈마 동적 모델의 이득값과 공정 장비가 가지는 실제 이득값의 이격에 의해 달라질 수 있다. 개발된 PI-APC를 적용한 공정 실험으로 실제 식각 산포가 개선되었으며, PI-APC 적용하지 않을 시, 공정 종료 후 80 nm 및 77 nm 높이 ck이를 가지는 SiO2 마스크 잔여 높이 및 Si 식각 깊이가 각각 4 nm 및 43 nm로 개선된 결과를 보였다.

공정 산포 및 플라즈마 분포를 대표하는 위치 간 차이 값의 형태를 가지는 PI 인자를 사용한 PI-APC 개발을 통해 단일 입력 단일 출력 (SISO) 형태의 다단 구조의 제어기가 플라즈마 이용 공정의 제어기로써 유효함을 보였다. 또한 이와 같은 구조의 PI-APC 운전을 통하여 공정 중 발생한 드리프트를 확인할 수 있었다. 이는 PI-APC를 통해 생성되는 장비-플라즈마 제어 데이터베이스(DB)가 공정 및 장비 개선의 기반 DB로써 활용될 수 있음을 보이는 결과이다.